

# Numerical Investigation of Pressure Drop at Turbulent Flow Conditions in Single Pellet String Reactors

Bachelor's Thesis

Student: Yong Sook Prasit Attavit  
Supervisor: Prof. Dr.-Ing. Kai-Olaf Hinrichsen  
Johanna Fernengel, M.Sc.

Date of Submission: March 16, 2020

# Abstract

Within this work, an existing investigation of pressure drop in various Single Pellet String Reactor (SPSR) set-ups is extended to cover turbulent flow. Two geometry-based weighting factors previously applied by Fernengel et al. are introduced to scale the influence of the confining wall in an equivalent diameter expression. It was concluded that in such narrow fixed-bed reactors, influence of the confining wall on pressure drop must be accounted for and the use of any of the proposed weighting factors on the Ergun equation will shift results closer to parity. Appropriate adjustments to include turbulent flow are made and ParaView is used to extract the pressure drop in previously proposed SPSR variations by Fernengel et al. With the exception of increasing superficial velocity and scaling factor in SPSR variations, the simulative pressure drop largely follows previously established trends from Fernengel et al.

The extracted simulative pressure drop values were compared against an aggregation of literature pressure drop correlations compiled by Erdim et al. A total of four plots pertaining to friction factor and pressure drop were plotted, and reasons for deviations from simulative values were discussed. It was observed from the results obtained that plotting the friction factor or pressure drop against normal Reynolds will, in general, lead to reduced values of friction factor and pressure drop respectively. It will not, however, change any observed trends when compared to their wall modified Reynolds counterparts. Most literature pressure drop correlations tend to underpredict simulative pressure drop within a SPSR in turbulent flow. This points to a need for specialised correlations relating to SPSR geometries to be developed, should predictions closer to parity be desired.

# Contents

<b>Abstract</b>	<b>ii</b>
<b>List of Figures</b>	<b>v</b>
<b>List of Tables</b>	<b>vi</b>
<b>List of Source-Codes</b>	<b>vii</b>
<b>Nomenclature</b>	<b>viii</b>
<b>1 Introduction</b>	<b>1</b>
<b>2 Theoretical Background</b>	<b>3</b>
2.1 Single Pellet String Reactors . . . . .	3
2.2 Numerical Simulation with CFD . . . . .	4
2.2.1 OpenFOAM as a CFD Program . . . . .	4
2.2.2 Turbulence Modelling . . . . .	5
2.2.3 $k-\omega$ -SST model . . . . .	8
2.2.4 The law of the wall . . . . .	10
<b>3 Model Description and Implementation</b>	<b>13</b>
3.1 Geometry . . . . .	13
3.2 Governing Equations . . . . .	16
3.3 Estimation on Turbulent Region in SPSRs . . . . .	17
3.4 Case set-ups . . . . .	18
3.4.1 Base Case . . . . .	18
3.4.2 Parameter Study . . . . .	19
3.4.3 Pressure Drop Correlations . . . . .	21
3.5 Adjustments related to Turbulent Flow . . . . .	22
3.6 Extraction of Pressure Drop Values From Simulations in ParaView . . . . .	24
<b>4 Results and Discussion</b>	<b>29</b>
4.1 Parameter Study . . . . .	29

4.2	Comparison to Literature . . . . .	33
4.2.1	Friction Factor . . . . .	33
4.2.2	Parity Plots . . . . .	36
<b>5</b>	<b>Conclusion</b>	<b>42</b>
<b>A</b>	<b>Bibliography</b>	<b>44</b>

# List of Figures

2.1	Plot of the dimensionless velocity, $u^+$ , against the dimensionless wall coordinate, $y^+$ , showing different zones of interest. . . . .	11
2.2	Slice of Base Case Showing Mesh Resolution. . . . .	12
3.1	Bottom section of a SPSR with trigonometric expressions used for analytical pellet positions. . . . .	14
3.2	Comparison of pressure drop across SPSR variations with Ergun and Blake-Kozeny using modified equivalent diameter. . . . .	17
3.3	Case A upon viewing with Paraview. . . . .	26
3.4	Case A after Cull FrontFace is activated. . . . .	26
3.5	First Slice made at the start of catalytic pellet string. . . . .	27
3.6	Second Slice made at the end of the catalytic pellet string. . . . .	27
3.7	Extraction of pressure values obtained from IntegrateVariables1, the relevant pressure values are highlighted. . . . .	28
3.8	Extraction of pressure values obtained from IntegrateVariables2, the relevant pressure values are highlighted. . . . .	28
4.1	Influence of fluid viscosity, flow velocity, diameter aspect ratio and geometry scaling factor on pressure drop. . . . .	29
4.2	Front view of case D3 highlighting meandering fluid flow. . . . .	31
4.3	Side view of case D3 highlighting fluid passing the particles in a straight manner perpendicular to the plane through the pellet centres. . . . .	31
4.4	Simulative and Literature Friction Factor against normal Reynolds number. . .	33
4.5	Simulative and Literature Friction Factor against wall modified Reynolds number. .	33
4.6	Parity plot for normal Reynolds in turbulent region, correlations as displayed by Erdim et al. . . . .	36
4.7	Parity plot for wall modified Reynolds in turbulent region, correlations as displayed by Erdim et al. . . . .	36
4.8	Parity plot showing the effects of weighting factors on cases with varying diameter aspect ratios, correlations obtained from Erdim et al. . . . .	37
4.9	Wall surface weighting factor as a function of diameter aspect ratio. . . . .	40

# List of Tables

3.1	Geometry and fluid properties of considered SPSRs. . . . .	19
3.2	Pressure drop correlations from literature. . . . .	21

# List of Source Codes

3.1	geometry . . . . .	15
3.2	fvSolution . . . . .	22

# Nomenclature

## Latin Symbols

$A$	area	$\text{m}^2$
$F_1, F_2$	blending functions	–
$x, y, z$	Cartesian coordinates	$\text{m}$
$D$	diameter of the confining cylinder	$\text{m}$
$d$	diameter of a catalytic pellet	$\text{m}$
$\eta$	dynamic viscosity	$\text{kg m s}^{-1}$
$\rho$	density of the fluid	$\text{kg m}^{-3}$
$A_t$	empty cross-sectional area of the reactor	$\text{m}^2$
$\nu$	kinematic viscosity of the fluid	$\text{m}^2\text{s}^{-1}$
$L$	length of the string of N particles	$\text{m}$
$d_m$	modified diameter	$\text{m}$
$n$	normal direction	$\text{m}$
$P$	normal/actual pressure	$\text{kg m}^{-1}\text{s}^{-2}$
$\varepsilon$	porosity of the reactor	–
$\Delta P$	pressure drop across the N number of catalytic pellets	$\text{kg m}^{-1}\text{s}^{-2}$
$P_k$	production limiter	–
$s$	scaling factor	–
$S$	surface area	$\text{m}^2$
$u_0$	superficial velocity	$\text{m s}^{-1}$
$p$	simulative pressure obtained in ParaView equivalent to pressure/density	$\text{m}^2\text{s}^{-2}$
$S$	tensor represented by the alphabet ' $S$ '	–
$k$	turbulence kinetic energy	–
$\omega$	turbulence specific dissipation rate	–
$I$	turbulence intensity to set in simulation	–
$S$	total surface area	$\text{m}^2$
$V$	total volume	$\text{m}^3$
$\bar{p}$	turbulent average property of pressure	$\text{kg m}^{-1}\text{s}^{-2}$
$v$	velocity	$\text{m s}^{-1}$



$V$	volume	$\text{m}^3$
$\dot{V}$	volumetric flow rate	$\text{m}^3\text{s}^{-1}$
$f$	weighting factor	–

### Greek Symbols

$\varepsilon$	mean bed porosity	–
$\eta$	dynamic viscosity	$\text{kg m}^{-1}\text{s}^{-1}$
$\nu$	kinematic viscosity	$\text{m}^2\text{s}^{-1}$
$\rho$	fluid density	$\text{kg m}^{-3}$
$\tau$	space time constant or residence time	s

### Subscript

p	catalytic pellet
eff	effective
mod	modified
ref	reference
t	turbulent
w	wall

### Dimensionless Numbers

Re	Reynolds Number
----	-----------------

### Abbreviations

CFD	computational fluid dynamics
SPSR	single pellet string reactor

### Operators

$\nabla$	divergence of a parameter	–
----------	---------------------------	---

# 1 Introduction

Fixed bed reactors play an important role in the chemical industry owing to their excellent behaviour with regards to low pressure drop and constructional simplicity [1]. They are applied in many unit operations such as cracking as well as catalytic and non-catalytic reactors. Gaining insight into fluid dynamic properties such as pressure drop and residence time, as well as species concentrations, is of great importance for optimal design of fixed bed reactors. Computational software packages such as OpenFOAM<sup>®</sup> can be used to study the hydrodynamic characteristics by numerical simulation with the possibility to include equations for species transport. The preferred turbulence model used in this work is the  $k-\omega$ -SST model after Menter et al. [2, 3]. SPSRs are a special type of fixed bed reactor where the confining wall of the reactor is only slightly larger than the diameter of the catalytic particles [4], which recently experienced a renewed interest [5–7].

The validation of pressure drop-flow rate relations for fixed-bed reactors have been a research topic for decades and is still continuing to be researched today [8]. An exception to this is the single pellet string reactor among the myriad of fixed-bed reactor types being researched and used in the industry. In a SPSR, spherical pellets are stacked alternatively on top of one another within a confining cylinder having a diameter which is slightly larger than the pellet itself. Although previously introduced by Scott et al. in the 1970s [4], SPSRs did not gain much recognition until recent publications revealed a renewed interest in this reactor concept, particularly its use for catalyst testing [5–7].

In a previous publication by Fernengel et al. [9], the characterization of conversion and residence time behaviour in SPSRs was achieved using numerical simulation and a design criterion comparing the reactor's performance to ideal plug flow was derived. In a subsequent work by the same author, the pressure drop behaviour in laminar flow of presented SPSRs variations is elaborated and compared with common literature correlations.

Pressure drop is related to the energy dissipated through the reactor bed due to fluid flow [10]. It is a hydrodynamic parameter that is of great interest to engineers as it can be used to determine energy losses, compression equipment size, liquid holdup, gas-liquid interfacial region and mass

transfer coefficients [11–13], all of which are important for the design and operation of various reactors.

In his thesis Ergun [14] analysed variables that led to pressure loss of flow across randomly packed beds. Amongst these variables investigated are fluid properties, velocity, particle characteristics as well as bed porosity. A correlation, coined as the Ergun equation, was then proposed for pressure drop in packed-beds and has since then remained as one of the most popular correlation for pressure drop.

The Ergun equation is divided into two terms affiliated with viscous and kinetic losses, each having a constant, which are commonly referred as the first and second Ergun coefficient. In laminar flow, the Ergun equation is reduced to the Blake-Kozeny equation due to predominant viscous losses [15, 16]. In turbulent flow however, the first term becomes close to negligible compared to the second term which becomes dominant.

It is important to note that the Ergun equation does not account for pressure losses owing to the confining wall. Pressure losses due to the confining wall become more prevalent and severe with the decrease in cylinder-to-particle diameter ratio  $D/d$ . As such, modifications to the original Ergun equation may have to be made to account for the low cylinder-to-particle diameter ratio which is a characteristic of SPSR. Following the approach by Fernengel et al. [17] in which the wall was incorporated into the equivalent diameter with a weighting factor, similar modifications are also adapted in this work. Such modifications included the use of equivalent diameters as characteristic length [4, 18], adjustments to the Ergun coefficients [19–21], and the usage of a new empirical correlation [22] to resolve the limitation of applying the original Ergun equation in a SPSR.

In this work, a numerical investigation of pressure drop in SPSRs is performed using computational fluid dynamics (CFD) simulation with the open-source program OpenFOAM<sup>®</sup>. The influence of fluid viscosity, flow velocity, diameter aspect ratio and scaling factor on the pressure drop of turbulent flow through SPSRs is evaluated and compared to results previously obtained in laminar flow [17]. A weighting factor is introduced to the equivalent diameter expression following Scott et al.’s approach [4] in an attempt to scale the influence of the confining wall surface, thereby improving the agreement between simulation results and Ergun-based pressure drop correlation. The simulative pressure drop values were also cross-referenced and discussed with respect to literature correlations (cf. Erdim et al. [8]).

It should also be noted that the geometry of the confining cylinder, parameters to be varied during parameter study and inert fines in this work are largely similar to [17]. Ultimately, the goal is to confirm and extend the range and validity of adjustments to the pressure drop correlation proposed by [17] in the turbulent region.

## 2 Theoretical Background

### 2.1 Single Pellet String Reactors

The concept of a reactor, in which pellets are packed into tubes of only slightly larger diameter, emerged in the 1960s and was named as single pellet string reactor by Scott et al. [4]. Therein, its resemblance to conventional packed beds with regards to flow behaviour was written in detail. The ease-of-use and convenience of SPSRs in a laboratory-scale for obtaining average diffusion coefficients across an array of temperatures and pressures with large porous particles was also highlighted.

In the chemical industry, the development, production and optimisation of new and existing heterogeneous catalysts plays a pivotal role. Performance evaluation of commercial catalysts is commonly accomplished at industrial process conditions, which requires the use of huge and expensive reactors with considerable gas flow rates, and with it, comes with the endangerment of engineers or technicians working on the reactor [23].

Thus, the general consensus would be to preferably achieve performance testing of catalysts at a much smaller scale. However, a multitude of problems such as axial convective and molecular diffusion, presents itself when attempting to downscale fixed-bed reactors, as presented by Sie [24]. Sie also cited the effectiveness of so-called *nanoflow reactors*, which were essentially reactors below the scale of microreactors, in the testing of industrial catalysts. This points towards the applicability of SPSRs.

Ultimately, the struggle is in finding a small reactor that has the capability to house industrial-sized catalysts and demonstrates hydrodynamics which are sufficiently close to optimal plug flow. As such, SPSRs may just fit the bill. The underlying principle of optimal plug-flow reactors is that lateral mixing is sufficient without any mixing in the longitudinal direction [25].

The idea of adding small inert particles to the catalytic bed which is present in this simulative work was put forward by both Sie [24] and Gierman [26]. In an attempt to improve the isothermal properties of catalytic fixed beds, Gierman [26] added small inert particles to the

catalytic bed which reduces wall effects and improves plug flow. While operating in trickle-flow, Sie [24] stated the need for the addition of fine particles in small beds of large industrial catalyst particles to ensure near plug flow hydrodynamics.

## 2.2 Numerical Simulation with CFD

Numerical simulation is a powerful, time-saving tool in which virtual models can be used to estimate the changes in parameters (such as pressure, temperature) across a stipulated physical and simulative time-frame. It is a form of simulation by which calculation is done on a computer with the user's choice of simulative program that implements a mathematical model for a physical system. Commonly used by data scientists and researchers, it is a powerful tool which leverage on the processing and computational power of computers to solve often complex non-linear systems of equations that will otherwise takes months to solve by conventional pen-and-paper methods. With the advent of numerical simulation, engineers and scientists alike would no longer have to go through various cycles of building and destroying physical prototypes of models to achieve the desired final products for their clients.

Computational Fluid Dynamics (CFD) software such as OpenFOAM<sup>®</sup> utilises a modelling technique that breaks down governing equations (continuity, momentum and energy) of fluid flow into simpler forms that can be solved via numerical techniques [27]. CFD then uses models to approximate some components of the flow. Since there are no universal rules or guidelines on the appropriateness of models to use, the burden is on the user to select the right model tailored to solve the desired problem on hand. Although computer modelling can be used to predict results, validation with experimental data is always necessary to verify the accuracy of the solution.

### 2.2.1 OpenFOAM as a CFD Program

OpenFOAM<sup>®</sup> is an acronym which stands for *Open Source Field Operation and Manipulation*. As the name implies, the program is open source and free in nature, meaning that its source code and libraries are available for users to edit and improve upon, thus thriving on the spirit of collaborative work from users on the Internet [28]. This signifies that users no longer have to spend long periods of time writing CFD codes or purchase (often) expensive commercial software. Through the solving of mathematical models, an approximation as to what happens in a single volume element (grid) in the simulative environment can be achieved, thus painting a picture as to what would be observed in reality.

The workflow of an OpenFOAM<sup>®</sup> simulation can be broken down into 3 main parts which are described briefly below:

1.) *Preprocessing*

*Mesh generation* is performed during this phase. In simpler cases, the use of the *blockMesh* utility is sufficient. In the case of more complicated geometries as in this study, a combination of *blockMesh*, *snappyHexMesh* and third-party programs such as Blender<sup>™</sup> can be used in the generation of the confining cylinder and the packing arrangement.

2.) *Solving*

As opposed to confining its users to a universal solver as typically seen in commercial CFD programs, OpenFOAM<sup>®</sup> does not have a generic solver applicable to all cases. Rather, the solvers present in OpenFOAM<sup>®</sup> are tailored to specific physics in the broad categories of different flow types and continuum mechanics that are, but not limited to: incompressible flow, compressible flow, multiphase flow, heat transfer and buoyancy-driven flows, particle-tracking flows and combustion [28]. In this case, the *simpleFoam* solver is used.

3.) *Postprocessing*

To produce graphical output of the simulated numerical values, OpenFOAM<sup>®</sup> uses an open-source, multiplatform data analysis and visualization application known as *ParaView*. In *ParaView*, users can utilise a plethora of postprocessing tools to visualise the change in parameters in the model throughout the iterative steps or physical time depending on the type of solver specified under the *solving* step.

## 2.2.2 Turbulence Modelling

Turbulence modelling is a technique to contrive a number of partial differential equations for turbulent-flow calculation, founded from approximation of the Navier-Stokes equation.

OpenFOAM<sup>®</sup> offers a wide range of turbulence simulation methods and models via its *TurbulenceModels* library. The library supports: models for constant and variable density (incompressible and compressible flows), inclusion of buoyancy terms (models for single and multiphase flows) and the configuration of sources and constraints in case input files. There are 3 main types of turbulence modelling present in OpenFOAM<sup>®</sup>, namely Reynolds-Averaged Simulation (RAS) or Reynolds-averaged Navier-Stokes (RANS), Direct Numerical Simulation (DNS), and Large Eddy Simulation (LES).

More often than not, turbulent flows are difficult to simulate owing to their randomness. The amount of information obtained from a simulation is directly proportional to the computational cost. Whilst LES and DNS offers a high degree of details, it requires prohibitively large simulation times. Mathematical expression and diffusion term of viscous stresses differ between Newtonian fluids and non-Newtonian fluids. Many turbulence models treat the effect of turbulence as an augmentation of mixing or diffusion. The modelled expression however, varies based on the selected turbulence models (linear eddy-viscosity, non-linear eddy viscosity, Reynolds-stress transport models under RANS).

In RANS, the Reynolds decomposition of the flow variables is accomplished by first separating the flow variables into mean and fluctuating parts [29]. Following which the Reynolds-decomposed variables are inserted into the Navier-Stokes equations. The averaging of the equations yields the Reynolds-stress tensor term, which has to be modelled for the RANS equations to be solved. Thus, additional (closure) equations are required to solve the system. These equations are derived from higher-order moments of the averaged Navier-Stokes equation with additional assumptions based on the knowledge of the properties of turbulent flow, resulting in a modified set of equations that is less-computationally intensive to solve [30]. An outline of the aforementioned steps is listed in the section below.

### 2.2.2.1 Reynolds Decomposition and Averaging

The following equations for the decomposition of flow variables in RANS are obtained from Alfonsi et al. [29]. The flow of a viscous incompressible fluid having constant properties is given by the Navier-Stokes equations:

$$\frac{\partial u_i}{\partial t} + \frac{\partial}{\partial x_j}(u_i u_j) = -\frac{\partial p}{\partial x_i} + \nu \frac{\partial^2 u_i}{\partial x_j \partial x_j} \quad (2.1)$$

$$\frac{\partial u_i}{\partial x_i} = 0 \quad (2.2)$$

where  $u_i$  is the fluid velocity,  $p$  being the pressure divided by the density  $\rho$ ,  $\nu$  is the fluid kinematic viscosity. Body forces do not appear explicitly, and the convective term of Equation (2.1) is being expressed in conservative form. The Reynolds decomposition in RANS proceeds via the decomposition of the dependent variables of Equations (2.1) and (2.2) into mean and fluctuating parts:

$$u_i = \bar{u}_i + u'_i, \quad p = \bar{p} + p' \quad (2.3)$$

under the assumption as proposed by Tennekes et al. [31], that the following properties of the average operator hold:

$$\overline{\phi'} = \overline{\psi'} = 0, \quad \overline{\phi\psi} = \overline{\phi}\overline{\psi} + \overline{\phi'\psi'}, \quad \overline{\overline{\phi}\phi'} = \overline{\overline{\psi}\psi'} = \overline{\overline{\phi}\psi'} = \overline{\overline{\psi}\phi'} = 0 \quad (2.4)$$

$$\overline{\phi^2} = \overline{\phi}^2 + \overline{\phi'^2}, \quad \frac{\partial \overline{\phi}}{\partial t} = \frac{\partial \overline{\phi}}{\partial t}, \quad \frac{\partial \overline{\phi}}{\partial x_i} = \frac{\partial \overline{\phi}}{\partial x_i} \quad (2.5)$$

with  $\phi$  and  $\psi$  being a representative of two generic flow variables. The mean value of any generic variable ( $\phi$ ) can be calculated, in a turbulent statistically steady state as a time average ( $\overline{\phi}^T$ ) and in a turbulent spatially homogeneous flow as a volume average ( $\overline{\phi}^V$ ). In a turbulent flow of a general nature the mean can be computed as an ensemble average:

$$\overline{\phi}^E(\mathbf{x}, t) = \lim_{N \rightarrow \infty} \frac{1}{N} \sum_{k=1}^N \phi^k(\mathbf{x}, t) \quad (2.6)$$

in which  $N$  represents the number of repeated experiments. In a turbulent statistically steady state and in a turbulent spatially homogeneous flow:

$$\overline{\phi}^T = \overline{\phi}^E, \quad \overline{\phi}^V = \overline{\phi}^E \quad (2.7)$$

Via substitution of Eq. 2.3 into Eqs. 2.1 and 2.2, taking an ensemble average and enforcing properties 2.4 and 2.5, a system of partial differential equations that governs the mean-velocity and pressure fields of incompressible turbulent flow is obtained as:

$$\frac{\partial \overline{u}_i}{\partial t} + \frac{\partial}{\partial x_j} (\overline{u}_i \overline{u}_j) = -\frac{\partial \overline{p}}{\partial x_i} + \nu \frac{\partial^2 \overline{u}_i}{\partial x_j \partial x_j} \quad (2.8)$$

$$\frac{\partial \overline{u}_i}{\partial x_i} = 0 \quad (2.9)$$

Referencing the nonlinear term of eqs. 2.8, one obtains:

$$\overline{u_i u_j} = \overline{(\overline{u}_i + u'_i)(\overline{u}_j + u'_j)} = \overline{\overline{u}_i \overline{u}_j} + \overline{\overline{u}_i u'_j} + \overline{u'_i \overline{u}_j} + \overline{u'_i u'_j} = \overline{u}_i \overline{u}_j + \overline{u'_i u'_j} \quad (2.10)$$

that gives:

$$\frac{\partial \overline{u}_i}{\partial t} + \frac{\partial}{\partial x_j} (\overline{u}_i \overline{u}_j) = -\frac{\partial \overline{p}}{\partial x_i} + \nu \frac{\partial^2 \overline{u}_i}{\partial x_j \partial x_j} - \frac{\partial}{\partial x_j} (\overline{u'_i u'_j}) \quad (2.11)$$



Thus, the RANS as projected by [32] is obtained:

$$\frac{\partial \bar{u}_i}{\partial t} + \bar{u}_j \frac{\partial \bar{u}_i}{\partial x_j} = -\frac{\partial \bar{p}}{\partial x_i} + \nu \frac{\partial^2 \bar{u}_i}{\partial x_j \partial x_j} - \frac{\partial \tau_{ij}}{\partial x_j} \quad (2.12)$$

$$\frac{\partial \bar{u}_i}{\partial x_i} = 0 \quad (2.13)$$

where the convective term of Eq. 2.12 is expressed in non-conservative form, and:

$$\tau_{ij} = \overline{u'_i u'_j} \quad (2.14)$$

gives the *Reynolds-stress Term* (*Reynolds-stress Tensor* divided by the density) which includes the effects of turbulent motions on the mean stresses.

The Reynolds-stress tensor is symmetric, and the diagonal components give the normal stresses, while the off-diagonal components are correlated to shear stresses. 2.12 and 2.13 are not a closed system for the calculation of the dependent variables,  $\bar{u}_i$  and  $\bar{p}$ , in the context that the Reynolds-stress tensor includes six additional independent unknowns. The problem with the closure of the Reynolds-averaged Navier-Stokes equations consists mainly in the formulation of the Reynolds-stress tensor as a function of the mean-field and/or other variables. Generally, turbulence models are designed to represent high-order moments of turbulence variability in lower-order moments. This can be done directly, as in the case of eddy viscosity models, or implicitly, as with the case of models based on the solution of additional partial differential equations.

In this study, RANS was considered to be the best turbulence model for the base case, as the increased computational load used for the depiction of eddies associated with the LES model would not be useful in obtaining an averaged pressure drop in a SPSR owing to its small confining diameter. It should be mentioned that the effectiveness of the RANS model requires careful monitoring of the  $y^+$  value, which is connected to the mesh refinement.

### 2.2.3 $k-\omega$ -SST model

The  $k-\omega$ -SST model is a linear eddy viscosity model stemmed from RANS. The turbulence model used in this work is the  $k-\omega$ -SST model, which is an extension of the standard  $k-\omega$  model widely popularised by Wilcox, D.C [33]. In the standard  $k-\omega$  model, two additional transport equations with variables  $k$  and  $\omega$  are introduced as a description of turbulent kinetic energy and the scale of turbulence respectively. The model by Wilcox is sensitive to the freestream

value of omega,  $\omega_f$ , thus leading to great deviations in the obtained simulative friction factor if an erroneous prediction of  $\omega_f$  is made and hence was not used in this study.

### 2.2.3.1 SST Model Formulation

The complete formulation of the SST model taken from Menter et al. [3] is outlined and modifications to the original  $k-\omega$  model are highlighted:

$$\frac{\partial(\rho k)}{\partial t} + \frac{\partial(\rho U_i k)}{\partial x_i} = \tilde{P}_k - \beta^* \rho k \omega + \frac{\partial}{\partial x_i} \left[ (\mu + \sigma_k \mu_t) \frac{\partial k}{\partial x_i} \right] \quad (2.15)$$

$$\frac{\partial(\rho \omega)}{\partial t} + \frac{\partial(\rho U_i \omega)}{\partial x_i} = \alpha \rho S^2 - \beta \rho \omega^2 + \frac{\partial}{\partial x_i} \left[ (\mu + \sigma_\omega \mu_t) \frac{\partial \omega}{\partial x_i} \right] + 2(1-F_1) \rho \sigma_{\omega 2} \frac{1}{\omega} \frac{\partial k}{\partial x_i} \frac{\partial \omega}{\partial x_i} \quad (2.16)$$

In which the blending function  $F_1$  is defined by:

$$F_1 = \tanh \left\{ \left\{ \min \left[ \max \left( \frac{\sqrt{k}}{\beta^* \omega y}, \frac{500\nu}{y^2 \omega} \right), \frac{4\rho \sigma_{\omega 2} k}{CD_{k\omega} y^2} \right] \right\}^4 \right\} \quad (2.17)$$

with  $CD_{k\omega} = \max \left( 2\rho \sigma_{\omega 2} \frac{1}{\omega} \frac{\partial k}{\partial x_i} \frac{\partial \omega}{\partial x_i}, 10^{-10} \right)$  and  $y$  is the distance to the nearest wall.

$F_1$  becomes zero away from the surface ( $k-\varepsilon$  model), and switches to one inside the boundary layer ( $k-\omega$  model). The turbulent eddy viscosity is defined as:

$$\nu_t = \frac{a_1 k}{\max(a_1 \omega, S F_2)} \quad (2.18)$$

where  $S$  is the invariant measure of the strain rate and  $F_2$  is a second blending function defined as:

$$F_2 = \tanh \left[ \left[ \max \left( \frac{2\sqrt{k}}{\beta^* \omega y}, \frac{500\nu}{y^2 \omega} \right) \right]^2 \right] \quad (2.19)$$

A production limiter is used in the SST model for the prevention of build-up of turbulence in stagnant regions:

$$P_k = \mu_t \frac{\partial U_i}{\partial x_j} \left( \frac{\partial U_i}{\partial x_j} + \frac{\partial U_j}{\partial x_i} \right) \rightarrow \tilde{P}_k = \min(P_k, 10 \cdot \beta^* \rho k \omega) \quad (2.20)$$

All constants are calculated by blending the corresponding constants from the  $k-\varepsilon$  and  $k-\omega$  model via  $\alpha = \alpha_1 F + \alpha_2 (1-F)$  etc. The constants for this model are:  $\beta^* = 0.09$ ,  $\alpha_1 = 5/9$ ,  $\beta_1 = 3/40$ ,  $\sigma_{k1} = 0.85$ ,  $\sigma_{\omega 1} = 0.5$ ,  $\alpha_2 = 0.44$ ,  $\beta_2 = 0.0828$ ,  $\sigma_{k2} = 1$ ,  $\sigma_{\omega 2} = 0.856$ . The only

modifications made from the original expression is the use of the strain rate,  $S$ , rather than the vorticity in Eq. 2.18, and the use of factor 10 in the production limiter, as opposed to 20 as proposed by Menter et al. [34, 35]. Although less sensitive to the freestream values of  $\omega$  as compared to the standard  $k-\omega$  model, an educated prediction of  $\omega$  must be done for the *simpleFoam* solver to work with.

Despite its popularity as a turbulence model used for practical calculations [36], the  $k-\varepsilon$ -model is not used in this work as it does not handle surface boundaries well.

The  $k-\omega$ -SST model used in OpenFOAM<sup>®</sup> is obtained from the 2003 model by Menter et. al. [3].

## 2.2.4 The law of the wall

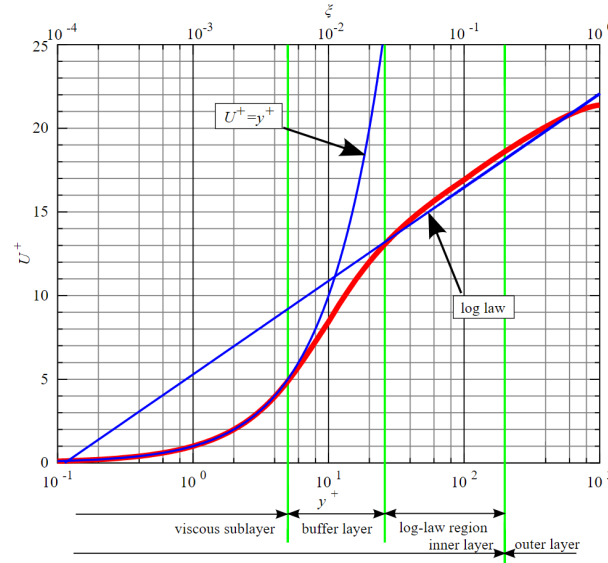
Due to large velocity gradients arising in the region near the wall, flow considered in the near-wall region is no longer turbulent. Thus, assumptions made while deriving the turbulence models are not applicable in this region.

The boundary layer velocity profile is subdivided into three regions through analytical equation derivations and experimental evidence fitting and is listed in order from increasing distance from the wall: the laminar sublayer, the buffer area, and the log-law zone [27, 37].

In the linear/laminar sublayer, the laminar law holds to which the dimensionless velocity is equals to the dimensionless wall coordinate (i.e.  $u^+ = y^+$ ). In this region, the fluid is dominated by viscous effects hence negligible Reynolds shear stress is assumed. In the log-law zone, turbulence stress dominates the flow and the velocity profile vary very slowly with the logarithmic function along the distance. In this region, the logarithmic law is valid and is given by  $u^+ = \ln(y^+)/\kappa + B$  where  $\kappa$  represents the Karman constant,  $\kappa = 0.41$ , and  $B$  the integration constant with  $B \approx 5.0-5.4$  [38, 39]. Laminar law is valid for  $y^+ < 5$  while logarithmic law is true for  $y^+ > 30$  up to  $y^+ = 500-1000$  [40].

A visual representation of the aforementioned zones is depicted in Fig. 2.1 [41]:

**Figure 2.1:** Plot of the dimensionless velocity,  $u^+$ , against the dimensionless wall coordinate,  $y^+$ , showing different zones of interest.



Two general approaches are usually employed in CFD when modelling the flow in the near-wall region, Low-Reynolds-number (low-Re) modelling and Wall function theory. In the Low-Re approach, the boundary layer is sufficiently fine meshed such that the first cell is placed entirely in the laminar sublayer of the boundary layer, with the height of the first cell corresponding to a value of  $y^+ \approx 1$  (although validity of laminar sublayer still holds true up till  $y^+ < 5$ ) [27], allowing the governing equations of fluid flow to be solved in all regions of the boundary layer.

In the second approach, the viscosity-affected inner region (with respect to the wall) which consists of the viscous sublayer and buffer layer is not resolved through fine mesh generation. Instead, the usage of semi-empirical wall functions are used to bridge the viscosity-affected region between the wall and the fully-turbulent region [30]. Wall functions are commonly used with coarser meshes in which the first cell is found at  $y^+ > 30$ . The use of wall functions avert the need for the modification of the turbulent models to account for the presence of the wall. This substantially saves computational resources in most high-Reynolds-number flows, because the near-wall region that is affected by viscosity, in which the solution variables change most rapidly, need not be resolved. As such, this approach is popular for near-wall treatment in industrial flow simulations because it is economical, robust, practical and reasonably accurate.

Having the height of the first cell land in the range of  $5 < y^+ < 30$  puts it in the buffer region, which is situated between the laminar sublayer and the log-law region of the boundary layer. It is generally not advisable to have the first cell land in this region as it amounts to less accurate results obtained with either of the two methods listed above [42].

Simulations on the base case were ran with and without wall functions being applied to  $k$ ,  $\omega$  and the model turbulent viscosity,  $\nu_t$ . In RANS, only the mean velocity  $\bar{u}$  is considered and the oscillating velocity term  $u'(t)$  is omitted thus leading to errors. Hence, the correct edition and inclusion of the model turbulent viscosity  $\nu_t$  is paramount to account for the transport and dissipation of energy neglected from the removal of  $u'(t)$ .

The effective viscosity,  $\nu_{eff}$ , in RANS as a function of the model turbulent viscosity and the physical viscosity thus given by:  $\nu_{eff} = \nu + \nu_t$

Due to the fineness of the mesh associated in the original base case as generated by Fernengel et al. [17], an extremely low  $y^+$  value in the range of  $y^+ < 2$  was obtained with  $k-\omega$ -SST with RANS simulation which places the height of the first cell in the laminar sublayer (cf. Fig. 2.2). A general rule of thumb when using wall functions is to obtain  $y^+$  values between 30 and 200 as this allows the first cell centre to be placed in the log-law region to ensure accuracy of the results.



**Figure 2.2:** Slice of Base Case Showing Mesh Resolution.

The  $\omega$  wall function is a special wall function that is able to switch between viscous and log-law region [43]. Furthermore, the  $k-\omega$ -SST by Menter has the ability to automatically shift from the standard low-Re formulation to wall function, based on grid spacing of the near-wall cell. Hence, using the turbulence model based on  $\omega$  (such as the  $k-\omega$ -SST model) should technically yield accurate results.

However, the obtained simulative results with wall functions yielded a pressure drop that gave a less-than-expected friction factor that does not correspond to friction factor values shown in Fig. 3.2. As such, it can be inferred that the  $k-\omega$ -SST model is best utilized without wall functions should a fine mesh be used as with this base case.

## 3 Model Description and Implementation

The simulations are based on a heterogeneous single pellet string reactor model, which integrates the solid particles with appropriate boundary conditions through the mesh. Due to negligible density changes, the fluid is assumed to be incompressible. Mesh generation and flow simulation are achieved with *snappyHexMesh* and *simpleFoam*, respectively, with OpenFOAM® v4.1 [44].

### 3.1 Geometry

In ideal conditions, catalytic pellets modelled by spherical particles are alternately stacked on top of each other on the opposite side of the walls in a SPSR (cf. Fig. 3.1). This allows the position of the catalytic pellets to be mathematically described based on the particle diameter  $d$  and the cylinder diameter  $D$  via Eqs. 3.1 and 3.2, when the z-x plane spans through the particle midpoints such that  $y_i = 0$ .

$$x_i = (-1)^i \left( \frac{D-d}{2} \right) \quad (3.1)$$

$$z_i = \frac{d}{2} + (i-1) \sqrt{d^2 - (D-d)^2} \quad (3.2)$$

The length  $L$  of the string of  $N$  particles can thus be given by Eq. 3.3.

$$L = d + (N-1) \sqrt{d^2 - (D-d)^2} \quad (3.3)$$

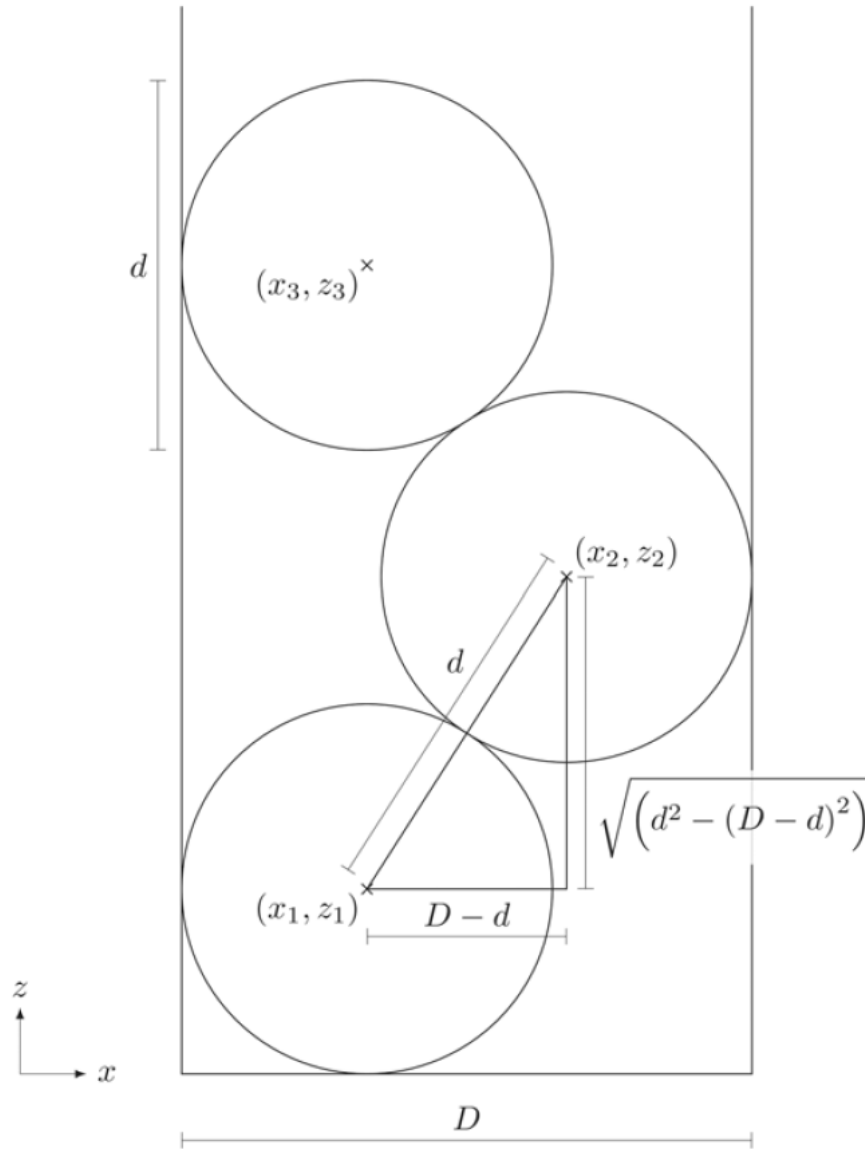


**Figure 3.1:** Bottom section of a SPSR with trigonometric expressions used for analytical pellet positions. Taken from Fernengel et al. [17] .

An excerpt of the codes used for the generation of the catalytic pellet string of  $N$  pellets is given by Sourcecode 3.1

**Sourcecode 3.1: geometry**

```

// snappyHexMesh sphere geometry
// parameters
d 0.0008; // sphere diameter
D 0.001; // cylinder diameter
r #calc "$d/2"; // sphere radius

// sphere coordinates
x0 #calc "($D-$d)/2*pow(-1,0)";
x1 #calc "($D-$d)/2*pow(-1,1)";
x2 #calc "($D-$d)/2*pow(-1,2)";
x3 #calc "($D-$d)/2*pow(-1,3)";
x4 #calc "($D-$d)/2*pow(-1,4)";
x5 #calc "($D-$d)/2*pow(-1,5)";
x6 #calc "($D-$d)/2*pow(-1,6)";
x7 #calc "($D-$d)/2*pow(-1,7)";
x8 #calc "($D-$d)/2*pow(-1,8)";
x9 #calc "($D-$d)/2*pow(-1,9)";
x10 #calc "($D-$d)/2*pow(-1,10)";
x11 #calc "($D-$d)/2*pow(-1,11)";
x12 #calc "($D-$d)/2*pow(-1,12)";
x13 #calc "($D-$d)/2*pow(-1,13)";
x14 #calc "($D-$d)/2*pow(-1,14)";
x15 #calc "($D-$d)/2*pow(-1,15)";
x16 #calc "($D-$d)/2*pow(-1,16)";
x17 #calc "($D-$d)/2*pow(-1,17)";
x18 #calc "($D-$d)/2*pow(-1,18)";
x19 #calc "($D-$d)/2*pow(-1,19)";

y 0;

z0 #calc "$d/2+sqrt(pow($d,2)-pow(($D-$d),2))*0+1.1*$d";
z1 #calc "$d/2+sqrt(pow($d,2)-pow(($D-$d),2))*1+1.1*$d";
z2 #calc "$d/2+sqrt(pow($d,2)-pow(($D-$d),2))*2+1.1*$d";
z3 #calc "$d/2+sqrt(pow($d,2)-pow(($D-$d),2))*3+1.1*$d";
z4 #calc "$d/2+sqrt(pow($d,2)-pow(($D-$d),2))*4+1.1*$d";
z5 #calc "$d/2+sqrt(pow($d,2)-pow(($D-$d),2))*5+1.1*$d";
z6 #calc "$d/2+sqrt(pow($d,2)-pow(($D-$d),2))*6+1.1*$d";
z7 #calc "$d/2+sqrt(pow($d,2)-pow(($D-$d),2))*7+1.1*$d";
z8 #calc "$d/2+sqrt(pow($d,2)-pow(($D-$d),2))*8+1.1*$d";
z9 #calc "$d/2+sqrt(pow($d,2)-pow(($D-$d),2))*9+1.1*$d";
z10 #calc "$d/2+sqrt(pow($d,2)-pow(($D-$d),2))*10+1.1*$d";
z11 #calc "$d/2+sqrt(pow($d,2)-pow(($D-$d),2))*11+1.1*$d";
z12 #calc "$d/2+sqrt(pow($d,2)-pow(($D-$d),2))*12+1.1*$d";
z13 #calc "$d/2+sqrt(pow($d,2)-pow(($D-$d),2))*13+1.1*$d";
z14 #calc "$d/2+sqrt(pow($d,2)-pow(($D-$d),2))*14+1.1*$d";
z15 #calc "$d/2+sqrt(pow($d,2)-pow(($D-$d),2))*15+1.1*$d";

```



z16	#calc "\$d/2+sqrt(pow(\$d,2)-pow((\$D-\$d),2))*16+1.1*\$d";	48
z17	#calc "\$d/2+sqrt(pow(\$d,2)-pow((\$D-\$d),2))*17+1.1*\$d";	49
z18	#calc "\$d/2+sqrt(pow(\$d,2)-pow((\$D-\$d),2))*18+1.1*\$d";	50
z19	#calc "\$d/2+sqrt(pow(\$d,2)-pow((\$D-\$d),2))*19+1.1*\$d";	51

From *system/geometry*, the three-dimensional position of the generated spheres are calculated based on the both the diameter of the confining cylinder and sphere  $D$  and  $d$ , respectively. However, the addition of inert fines to the SPSR has to be achieved by the software Blender™ 2.76b [45] as its positions can no longer be analytically described anymore. The particle deposition and settling algorithm in the bed relies on collision detection and resolution based on rigid body physics, which is made available through the incorporation of the Bullet Physics Library [46].

The reactor length is ascertained by the number and size of the spherical particles, as well as the cylinder-to-particle diameter ratio. Additionally, a small bed of inert fines is placed at the inlet of the SPSR, upstream of the catalytic pellet string to fit possible experimental set-ups whilst enforcing near-plug flow to prohibit back-mixing in the entry zone.

## 3.2 Governing Equations

*simpleFoam* is a steady-state solver that was chosen to handle the base case system. The acronym SIMPLE stands for Semi-Implicit Method for Pressure Linked Equations. With reference to Fernengel et al. [17], turbulent flow of incompressible isothermal fluids at steady-state with *simpleFoam* can be described by the governing equations of momentum and continuity. For incompressible cases, the continuity equation is simplified to the point at which the divergence of the velocity is equals to 0 as depicted in Eq. 3.4 below:

$$\nabla \cdot \mathbf{u} = 0 \quad (3.4)$$

$$\nabla \cdot (\mathbf{uu}) = -\frac{1}{\rho} \nabla p + \nu \nabla^2 \mathbf{u} \quad (3.5)$$

$$p = \frac{1}{\rho} P \quad (3.6)$$

where  $\mathbf{u}$  represents the velocity vector,  $\rho$  the density of the fluid,  $\nu$  representing the kinematic viscosity. It is also important to note that the pressure  $p$  used in the simulations is not the actual pressure, but rather the reciprocal of the density  $\rho$  multiplied by the actual pressure  $P$  as depicted

in Eq. 3.6 above. No-slip is defined at both the wall and particle surfaces ( $u_s = 0 \text{ m s}^{-1}$ ) and the remaining boundaries are set to zero gradient normal to the boundary ( $\partial/\partial n = 0$ ).

For  $k-\omega$ -SST turbulence modelling in OpenFOAM<sup>®</sup>, the input of initial values of  $k$ ,  $\nu_{\text{t}}$ ,  $\omega$ ,  $p$  and  $U$  in the 0/ folder is necessary for accurate RANS simulation to proceed. Prediction of the initial estimates for the turbulence kinetic energy,  $k$ , and turbulence specific dissipation rate,  $\omega$ , can be approximated via Eqs. 3.7 and 3.8 [47]

$$k = \frac{3}{2}(I|u_{\text{ref}}|)^2 \quad (3.7)$$

$$\omega = \frac{k^{0.5}}{C_\mu L} \quad (3.8)$$

where  $I$  is the turbulence intensity,  $u_{\text{ref}}$  the reference velocity corresponding to the superficial velocity at the inlet,  $C_\mu$  being a constant which is equivalent to 0.09 and  $L$  being the reference length scale which in this case corresponds to the inner diameter of the confining cylinder.

The turbulence intensity was assumed to be 5% as this case corresponds to a medium-turbulence case, which commonly occurs in flows present in pipes.

### 3.3 Estimation on Turbulent Region in SPSRs

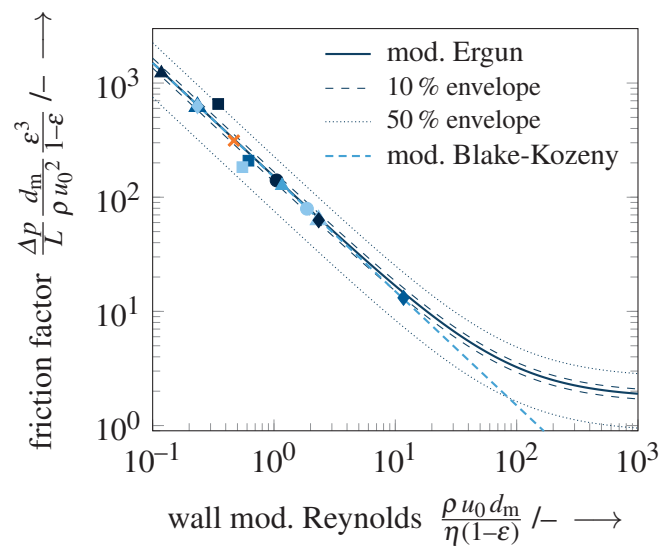


**Figure 3.2:** Comparison of pressure drop across SPSR variations with Ergun [14] and Blake-Kozeny [15, 48] equation with a modified equivalent diameter [4]. Taken from Fernengel et al. [17].

A plot of friction factor against wall modified Reynolds is useful in determining the range of wall modified Reynolds in which the simulation lands within the turbulent region of interest. With increasing wall modified Reynolds value, a sharp decrease, followed by a gradual and finally plateauing (almost constant) value of friction factor will usually be observed. An educated initial estimate for a turbulent wall modified Reynolds value was achieved with Fig. 3.2.

In this case, the initial value of  $u_0$  was calculated from a wall modified Reynolds value of  $2 \cdot 10^3$ , which places the simulation in the turbulent region. The estimation of  $u_0$  was achieved by rearranging Eq. 3.9 to set  $u_0$  as the subject:

$$Re_{\text{mod}} = \frac{\rho u_0 d_m}{\eta(1-\varepsilon)} \quad (3.9)$$

To obtain the corresponding friction factor ( $f_p$ ) from  $u_0$ , the obtained pressure drop from simulation ( $\Delta P$ ) along with the equivalent diameter, density, length of the catalytic pellet string and porosity was substituted into the equation below:

$$f_p = \frac{\Delta P}{L} \frac{d_m}{\rho u_0^2} \frac{\varepsilon^3}{1-\varepsilon} \quad (3.10)$$

## 3.4 Case set-ups

### 3.4.1 Base Case

The base case in this work corresponds to case A in [17].

Both inert fines and catalytic pellets are assumed to be spherical, non-porous and having a smooth surface. The cylindrical tube acts as a confining wall. The fluid is introduced into the SPSR at the inlet. A constant space time  $\tau$ , defined as the ratio of the fluid volume ( $V_f$ ) surrounding the catalytic particles to the volumetric flow rate  $\dot{V}$ , is maintained across the catalytic bed. The resulting superficial velocity,  $u_0$ , dependent on the reactor is thus given by Eq. 3.11 as shown below:

$$u_0 = \frac{\dot{V}}{A_t} = \frac{V_f}{A_t \tau} = \frac{L - \frac{V_p}{A_t}}{\tau} = \frac{d + (N-1)\sqrt{d^2 - (D-d)^2} - \frac{2Nd^3}{3D^2}}{\tau} \quad (3.11)$$

where  $A_t$  is the SPSR's empty cross-sectional area and  $V_p$  corresponds to the total volume occupied by the catalytic pellets.

In the base case set-up, 20 catalytic pellets ( $N = 20$ ) each having a diameter of  $d = 0.8$  mm are arranged as a single pellet string within a confining cylinder tube having an inner diameter of  $D = 1.0$  mm. A short bed of inert fines with a diameter of  $d/5$  are placed upstream of the catalytic pellet, close to the inlet of the SPSR. A fluid having a viscosity of  $\nu = 1.529 \cdot 10^{-5}$  m<sup>2</sup>/s with a density of  $\rho = 1.2506$  kg m<sup>-3</sup> enters the SPSR from the inlet and passes the catalytic bed with a space time of  $2.34 \cdot 10^{-4}$  seconds, thereby expecting turbulent flow through the reactor. To investigate the influence of fluid viscosity, flow velocity and reactor geometry on the pressure drop in a SPSR, parameters are varied in the base case set-up according to Tab. 3.1.

### 3.4.2 Parameter Study

**Table 3.1:** Geometry and fluid properties of considered SPSRs.

Case	Number of particles	Particle Diameter [mm]	Cylinder diameter [mm]	Viscosity
A	20	0.8	1.0	$\nu$
B1	20	0.8	1.0	$0.2\nu$
B2	20	0.8	1.0	$0.04\nu$
B3	20	0.8	1.0	$2\nu$
C1	5	0.8	1.0	$\nu$
C2	10	0.8	1.0	$\nu$
C3	50	0.8	1.0	$\nu$
C4	100	0.8	1.0	$\nu$
D1	20	0.8	0.9	$\nu$
D2	20	0.8	1.2	$\nu$
D3	20	0.8	1.4	$\nu$
E1	20	1.2	1.5	$\nu$

The following simulations were ran at a wall modified Reynolds number of  $2 \cdot 10^3$ , which signifies a turbulent flow via cross-referencing with Fig. 3.2 as it corresponds to a plateau in the  $f_p$  value in the graph with further increases in the wall modified Reynolds number. For accurate comparison of the conversion of a chemical reaction in a SPSR, the calculated residence time at a wall modified Reynolds value of  $2 \cdot 10^3$ , dubbed as  $\tau_{turbulent}$ , was kept constant whilst selected parameters were altered to study their effects on pressure drop. Parameters of all of the considered reactor variations are provided in Tab. 3.1.

#### 3.4.2.1 Influence of Fluid Viscosity

The influence of fluid viscosity on pressure drop can be determined through variation of the fluid viscosity passing through the SPSR. The modification of fluid viscosity was achieved

by changing the values of  $v$  located in *constant/transportProperties*. The modified cases with  $v = 0.2v$ ,  $0.04v$  and  $2v$  correspond to Case B1, B2 and B3.

#### 3.4.2.2 Influence of Flow Velocity

To measure the influence of flow velocity on pressure drop, the number of pellets in the string of catalytic pellets,  $N$  is changed accordingly from the base case. As the length of the string of catalytic pellets,  $L$ , is a function of  $N$  new values of both  $L$  and  $L_{\text{confining cylinder}}$  must be keyed into *system/geometry* and *constant/polyMesh/blockMeshDict* in the *snappyHexMesh* folder respectively. The length of the confining cylinder to be generated can be calculated as per Eq. 3.12 below and  $L$  with Eq. 3.3

$$L_{\text{confining cylinder}} = L + 2.2d \quad (3.12)$$

Next, the geometry of the bed of inert fines generated by Blender™ must be scaled and shifted. This can be accomplished through the *surfaceTransformPoints – translate* command to shift the inert bed to its correct geometric position between cases accordingly.

The superficial velocity for the modified cases in which  $N = 5, 10, 20, 50$  and  $100$  corresponding to Case C1, C2, C3 and C4 at a wall modified Reynolds of  $2 \cdot 10^3$  were calculated with Eq. 3.11 using  $\tau_{\text{turbulent}}$ .

#### 3.4.2.3 Influence of Diameter Aspect Ratio and Geometry Scaling Factor

For the investigation of the influence of diameter aspect ratio and geometry scaling factor on pressure drop, new inert bed of particles had to be regenerated with Blender™ owing to the change in the diameter of the confining cylinder. Cases D1, D2 and D3 are related to the diameter aspect ratio while cases E1 and E2 are related to the geometry scaling factor.

### 3.4.3 Pressure Drop Correlations

Author(s)	Relation	Equation	Range of applicability
Ergun	$f_p = (150 + 1.75(\frac{Re}{1-\varepsilon})) \frac{(1-\varepsilon)^2}{\varepsilon^3 Re}$	1	$0.2 < Re_1 < 700$
Avontuur and Geldart	$f_p = (141 + 1.52(\frac{Re}{1-\varepsilon})) \frac{(1-\varepsilon)^2}{\varepsilon^3 Re}$	2	$Re_m < 10,000$
Kuo and Nydegger	$f_p = (276.23 + 5.05(\frac{Re}{1-\varepsilon})^{0.87}) \frac{(1-\varepsilon)^2}{\varepsilon^3 Re}$	3	$460 < Re < 14,600$
Jones and Krier	$f_p = (150 + 3.89(\frac{Re}{1-\varepsilon})^{0.87}) \frac{(1-\varepsilon)^2}{\varepsilon^3 Re}$	4	$1000 < Re < 100,000$
Lee and Ogawa	$f_p = 6.25(\frac{29.32}{Re} + \frac{1.56}{Re^n} + 0.1) \frac{(1-\varepsilon)^2}{\varepsilon^3}$ $n = 0.352 + 0.1\varepsilon + 0.275\varepsilon^2$	5	$1 < Re < 400,000$
O'Neill and Benyahia	$f_p = (A + B(\frac{Re}{1-\varepsilon})) \frac{(1-\varepsilon)^2}{\varepsilon^3 Re}$ $A = 521.26 - 22581.24/(D/d_p)^2$ $B = 1.12 + 4.2/(D/d_p)$	6	$5 < D/d < 25$

**Table 3.2:** Pressure drop correlations from literature [8].

In this work, only the pressure drop over the length of catalytic pellet string is to be considered. Pressure drop across the SPSR obtained from the simulations are compared to the Ergun equation and is given by Eq. 3.13 below.

$$\frac{\Delta p}{L} = 150 \frac{(1-\varepsilon)^2}{\varepsilon^3} \frac{\eta u_0}{d^2} + 1.75 \frac{1-\varepsilon}{\varepsilon^3} \frac{\rho u_0^2}{d} \quad (3.13)$$

in which  $\Delta p/L$  is defined as the pressure drop across the bed per unit length,  $\varepsilon$  is the bed porosity, where  $\eta$  is the dynamic viscosity of the fluid. The first term in Eq. 3.13 describes the contribution of viscous losses which are prevalent in laminar flow, while the second term illustrates kinetic energy losses dominant in turbulent conditions. With reference to both Scott et al. and Lee et al. [4, 49], a modified equivalent diameter  $d_m$  involving the wall surface  $S_w$ , total pellet surface  $S_p$  and the total pellet volume  $V_p$  is used as the characteristic length. This modified equivalent diameter is depicted in Eq. 3.14 as such:

$$d_m = \frac{6V_p}{S_p + S_w} \quad (3.14)$$

Erdim et al. have compiled, evaluated and constituted a uniform notation to assist in comparisons in the calculation of pressure drop caused by fluid flow through packed beds [8].

With reference from Tab. 3.2 in Erdim et al. [8], suitable literature correlations whose Reynolds number (or diameter aspect ratio) lies within this work's simulative range of wall modified Reynolds number were considered, and their corresponding friction factors were evaluated. The "modified particle friction factor" formula suggested by Montillet et al. [50] was employed to obtain the pressure drop by correlation through the rearrangement of Eq. 3.15:

$$f_p = \frac{-\Delta P d_p}{\rho V^2 L} = f_k \frac{(1-\varepsilon)}{\varepsilon^3} = f_v \frac{(1-\varepsilon)^2}{\varepsilon^3 Re} \quad (3.15)$$

### 3.5 Adjustments related to Turbulent Flow

Extensive simulative runs with different *fvSolution* settings were made in a attempt to find the best configuration for accurate depiction of pressure drop in turbulent flow in the base case. The *fvSolution* (cf. [17]) was edited with reference to the motorBike tutorial provided in OpenFOAM® as it uses the RANS  $k-\omega$ -SST model by default, and uses the *simpleFoam* solver for incompressible flow. After much testing, a combination of settings borrowed from both Fernengel et al. [17] and the motorBike tutorial's *fvSolution* was employed in the base case. The edited *fvSolution* used in all simulations is depicted in Sourcecode 3.2 below:

**Sourcecode 3.2:** fvSolution

```

/*-----* C++ -*-----* \ 1
| ===== | 2
| \ \ / F i e l d | OpenFOAM: The Open Source CFD Toolbox | 3
| \ \ / O p e r a t i o n | Version: 2.4.0 | 4
| \ \ / A n d | Web: www.OpenFOAM.org | 5
| \ \ / M a n i p u l a t i o n | 6
\*-----*/ 7
FoamFile 8
{ 9
    version 2.0; 10
    format ascii; 11
    class dictionary; 12
    object fvSolution; 13
} 14
// * * * * * 15
    * * * * * // 16
solvers 17
{ 18

```

```

p                                     19
{                                     20
    solver                           GAMG;                               21
    tolerance                         1e-7;                             22
    relTol                           0.01;                             23
    smoother                         GaussSeidel;                       24
    nPreSweeps                        0;                                 25
    nPostSweeps                       2;                                 26
    cacheAgglomeration on;                                                 27
    agglomerator                      faceAreaPair;                     28
    nCellsInCoarsestLevel 10;                                             29
    mergeLevels                       1;                                 30
}                                     31
                                     32
Phi                                   33
{                                     34
    $p;                             35
}                                     36
                                     37
U                                     38
{                                     39
    solver                           smoothSolver;                     40
    smoother                         GaussSeidel;                       41
    tolerance                         1e-8;                             42
    relTol                           0.1;                             43
    nSweeps                          1;                                 44
}                                     45
                                     46
k                                     47
{                                     48
    solver                           smoothSolver;                     49
    smoother                         GaussSeidel;                       50
    tolerance                         1e-8;                             51
    relTol                           0.1;                             52
    nSweeps                          1;                                 53
}                                     54
                                     55
omega                                56
{                                     57
    solver                           smoothSolver;                     58
    smoother                         GaussSeidel;                       59
    tolerance                         1e-8;                             60
    relTol                           0.1;                             61
    nSweeps                          1;                                 62
}                                     63
}                                     64
                                     65
SIMPLE                               66

```



```

{
    nNonOrthogonalCorrectors 0;
}

potentialFlow
{
    nNonOrthogonalCorrectors 10;
}

relaxationFactors
{
    fields
    {
        p            0.3;
    }
    equations
    {
        U            0.7;
        k            0.7;
        omega        0.7;
    }
}

cache
{
    grad(U);
}

```

### 3.6 Extraction of Pressure Drop Values From Simulations in ParaView

Mesh generation for the base case and subsequent cases are accomplished using a combination of snappyHexMesh and Blender™. The steady-state solver *simpleFoam* was then used to iterate and solve for velocity, pressure,  $k$ , omega and nut values. Since OpenFOAM® does not have a Graphical User Interface, postprocessing of the calculated results were achieved using ParaView v5.6.0.

The *ParaView* command was used in the terminal to view the *.foam* file of the relevant case. For demonstration purposes in this chapter, the base case, Case A, was used as the model. Outlined below is the general procedure used to obtain the simulative pressure drop for all cases.

- 1.) The relevant case was viewed in ParaView as shown in Fig. 3.3
- 2.) In order to accurately approximate the location of the slices to be made, the 'Backface Representation' was switched from "Follow Frontface" to "Cull FrontFace". Fig. 3.4 shows Case A after Cull FrontFace is activated.
  - For an accurate approximation of the slice location, "Axes Grid" was ticked under Annotations to gauge where the slice is made.
- 3.) The "Slice" command was utilised with the Slice Type set to "Plane". It was used to generate a slice normal to the Z-axis at two locations. The first location corresponding to Slice 1 was made just downstream of the inert fines, in the small gap between the inert fines and the entrance of the string of catalytic pellets. The second slice, Slice 2 was made after the string of catalytic pellets, upstream of the exit of the SPSR. Fig. 3.5 and 3.6 shows Slice 1 and Slice 2 being made in the SPSR respectively.
  - The "Slice" Command can be found under Filters -> Alphabetical -> Slice
- 4.) Two separate "IntegrateVariables" commands corresponding to IntegrateVariables1 and IntegrateVariables2 were applied on both Slice 1 and Slice 2.
  - The "IntegrateVariables" command can be found other Filters -> Alphabetical -> Integrate Variables.
- 5.) Following which the relevant pressure values were extracted from IntegrateVariables1 and IntegrateVariables2 using the Spreadsheet View with the Attribute: Cell Data. Fig. 3.7 and 3.8 showcases the relevant integrated pressure values obtained from IntegrateVariables1 and IntegrateVariables2 respectively.

It is important to note that the Integrate Variable filter only integrates a given variable in this one area, and that the filter can be likened to:  $\int p dA = \int \int p dx dy$  as in this case, where the variable extracted is the pressure. Thus, the following steps are required to obtain the actual pressure drop across the SPSR:

- 1.) The obtained pressure in this case being  $\int p dA$  from IntegrateVariables 1 and 2 were each divided by the area of the cross-section of the confining cylinder to yield two values of  $p$ .
- 2.) The difference of both  $p$  values was taken, multiplied by the density of the fluid and then divided by the length of the confining cylinder,  $L$  to finally obtain the actual pressure drop per unit length across the SPSR.

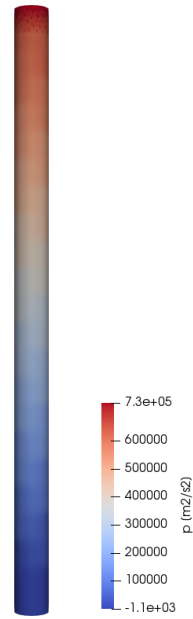


**Figure 3.3:** Case A upon viewing with Paraview.

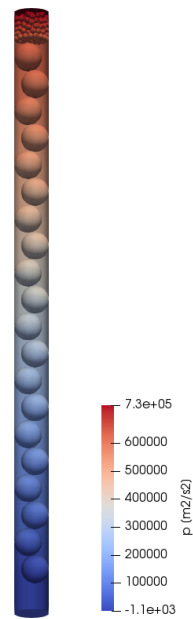


**Figure 3.4:** Case A after Cull FrontFace is activated.

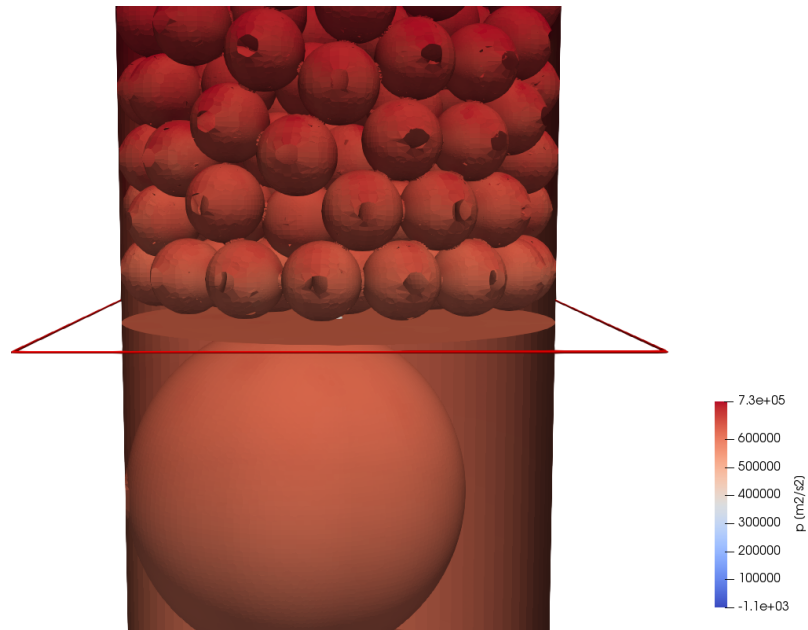


**Figure 3.5:** First Slice made at the start of catalytic pellet string.

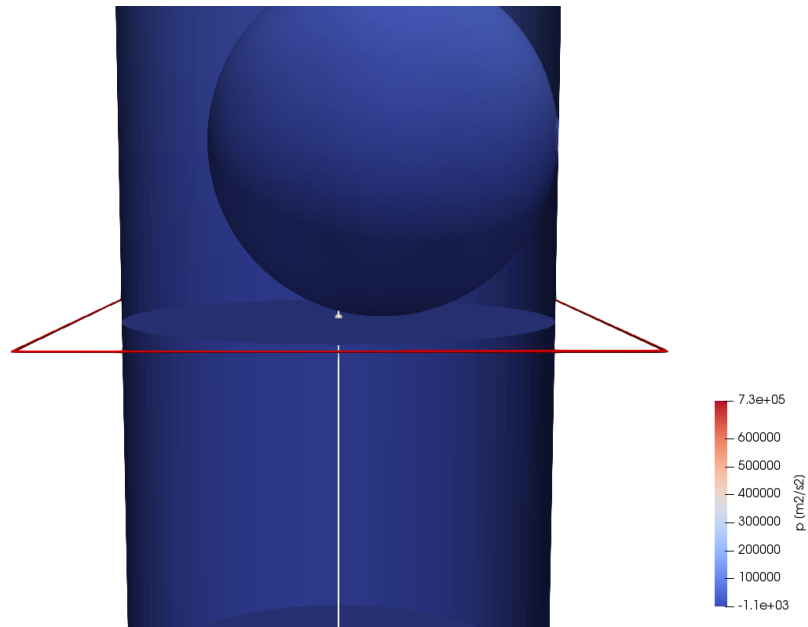


**Figure 3.6:** Second Slice made at the end of the catalytic pellet string.

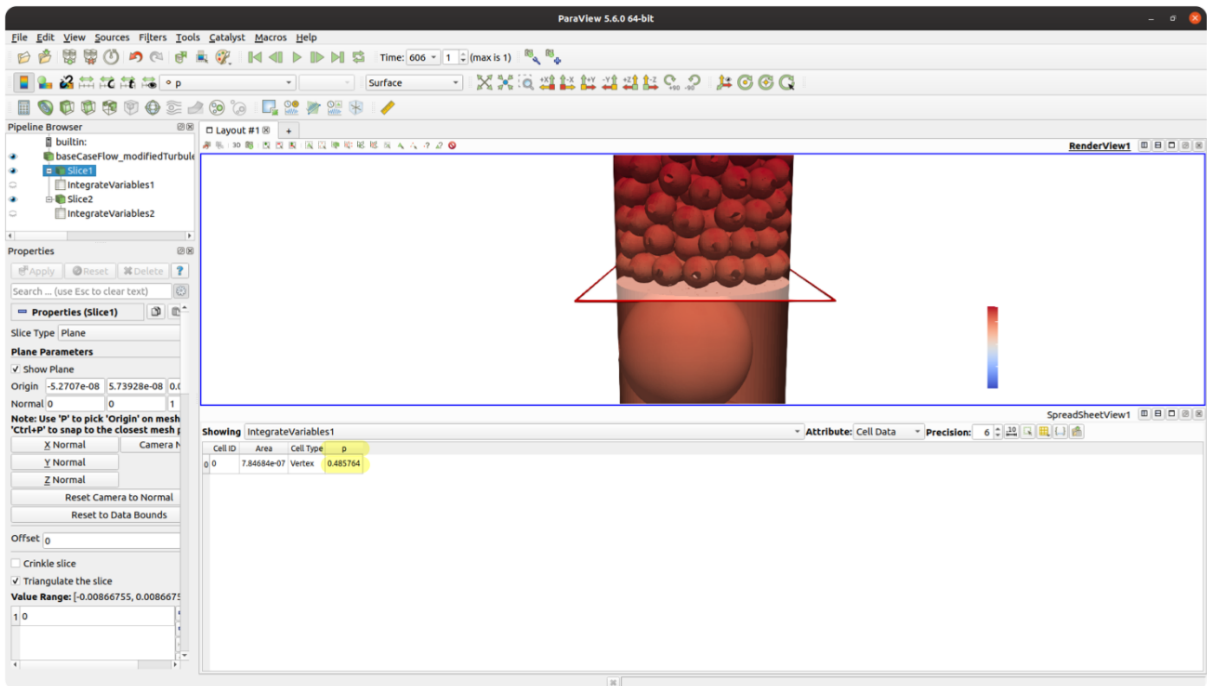


**Figure 3.7:** Extraction of pressure values obtained from IntegrateVariables1, the relevant pressure values are highlighted.

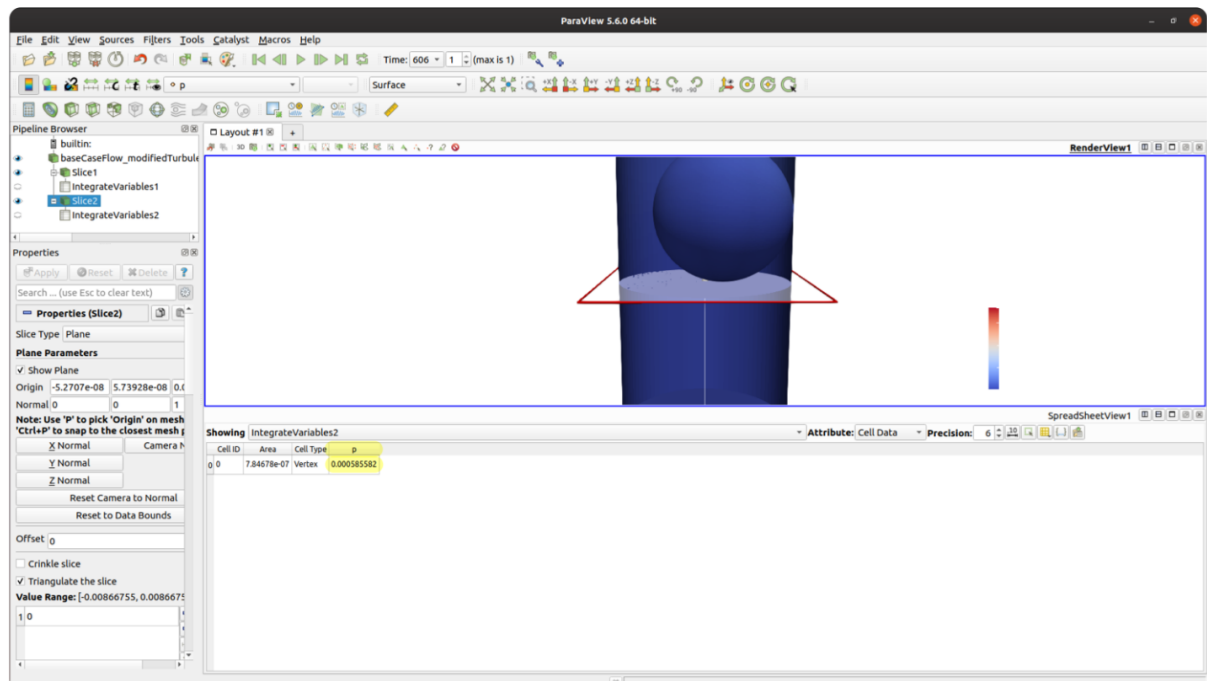


**Figure 3.8:** Extraction of pressure values obtained from IntegrateVariables2, the relevant pressure values are highlighted.

## 4 Results and Discussion

### 4.1 Parameter Study

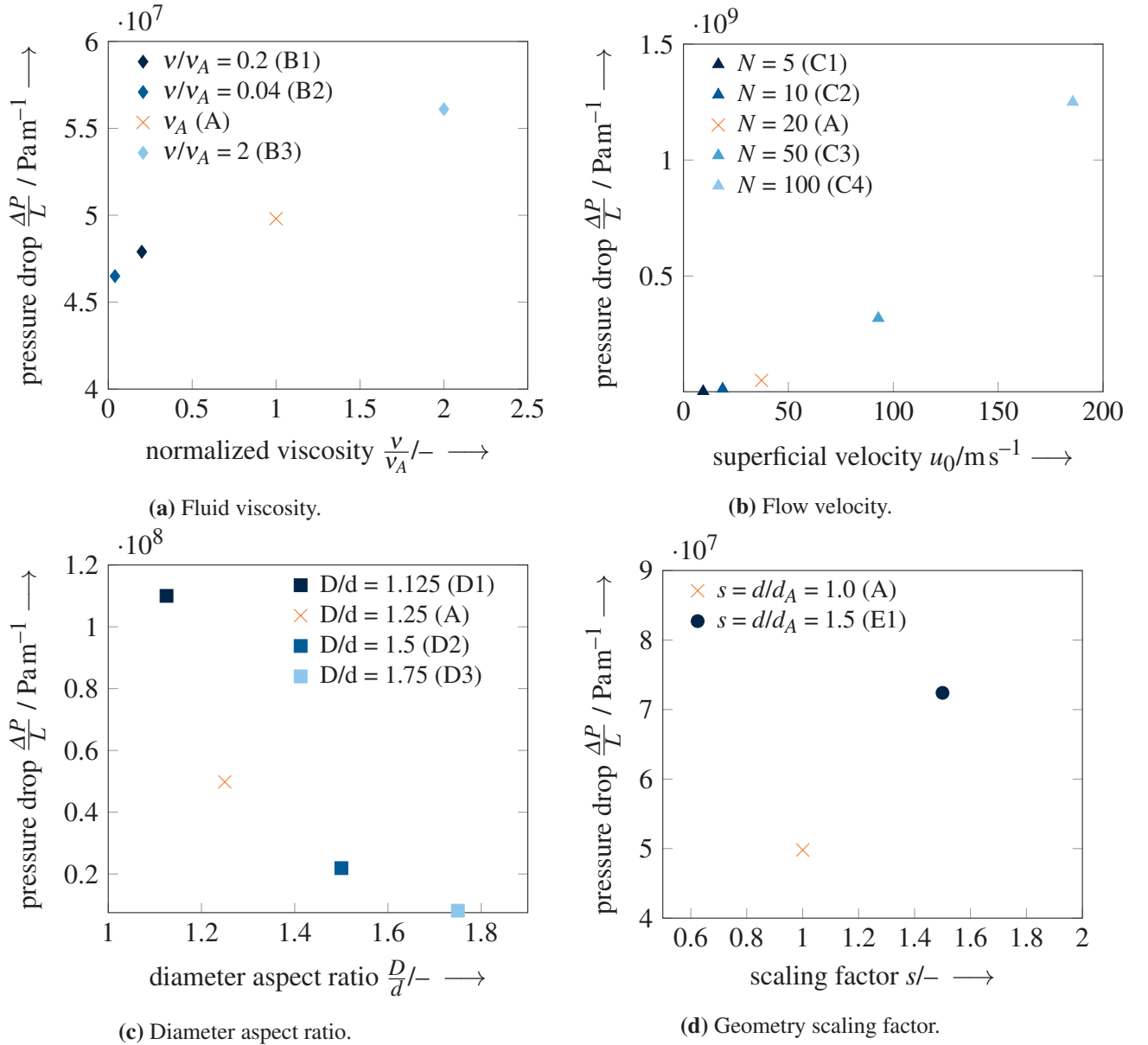


**Figure 4.1:** Influence of fluid viscosity, flow velocity, diameter aspect ratio and geometry scaling factor on pressure drop.

Fig. 4.1a shows an almost linear relationship between pressure drop and fluid viscosity, with less-than-expected values for pressure drop obtained at elevated levels of normalized viscosity at  $\frac{\nu}{\nu_A} = 1$  and  $\frac{\nu}{\nu_A} = 2$  respectively. As mentioned previously above, the first term of the Ergun equation (cf. Eq. 3.13) is mostly decisive at laminar flows and it corresponds to viscous losses. Having a wall modified Reynolds value of  $2 \cdot 10^3$  enables turbulent simulative flow, in which the second term of the Ergun equation relating to kinetic losses becomes more dominant. Thus, a reason for the lower-than-expected values for higher normalized viscosity values of 1 and 2 thereby causing a deviation from the linear relationship observed in Fernengel et al. [17] may be due to this dominant second term in turbulent flow, in which viscous losses are less dominant at elevated values of normalized viscosity. The observed trend can be also explained mathematically: Viscous losses represented by the dynamic viscosity term ( $\eta$ ) is not present in the predominant second Ergun coefficient in turbulent flow.

Looking at Fig. 4.1b, an exponential increase in pressure drop with rising superficial velocity was observed as opposed to the linear trend discovered previously in laminar flow (cf. [17]). This obtained results are in line with a similar simulative study performed in a two-dimensional SPSR at turbulent conditions by Müller et al. [51]. Synonymous to Müller et al., the slope of the pressure drop against velocity graph becomes increasingly steeper and non-linear at elevated superficial velocities and eventually displays an exponential trend. The increase in superficial velocity and hence pressure drop values with the addition of catalytic pellets in the SPSR can be explained both mathematically and theoretically. From a mathematical point of view, with reference to Eqs. 3.11 and 3.13: An increase in  $N$  will lead to an surge in  $u_0$  (ref. Eq. 3.11), which indirectly raises the  $\Delta P/L$  value (ref. Eq. 3.13). From a theoretical point of view, higher frictional forces between the fluid and particles will arise from increased fluid velocities thus leading to increased values of pressure drop [51].

The effects of varying diameter aspect ratio on pressure drop over the pellet string is depicted in Fig. 4.1c. Here, we observe trends similar with what was ascertained in laminar flow (cf. Fernengel et al. [17]) with respect to the reduction in pressure drop with increasing diameter aspect ratio. An increment in diameter aspect ratio (from  $D/d = 1.125$  to  $1.25$ ) projects a greater-than threefold sharp reduction in pressure drop similar to what was observed in laminar flow. Following which, further increases in the diameter aspect ratio (from  $D/d = 1.25$  to  $1.75$ ) leads to a less aggressive reduction in pressure drop. This pattern is predicted as there are two major flow pathways occurring in the SPSRs: one meandering around the pellets flowing from one side of the bed to the other, and the other passing the particles in a straight manner perpendicular to the plane through the pellet centres. Such flow channels adjacent to the pellet string are more prominent with increasing diameter aspect ratios, contributing to higher bed porosities for the proposed reactor geometries [17] which mathematically leads to lower pressure drop values (referencing Eq. 3.13). The aforementioned two major flow pathways are highlighted and displayed with ParaView using Case D3 as a reference model in Figs. 4.2 and 4.3.

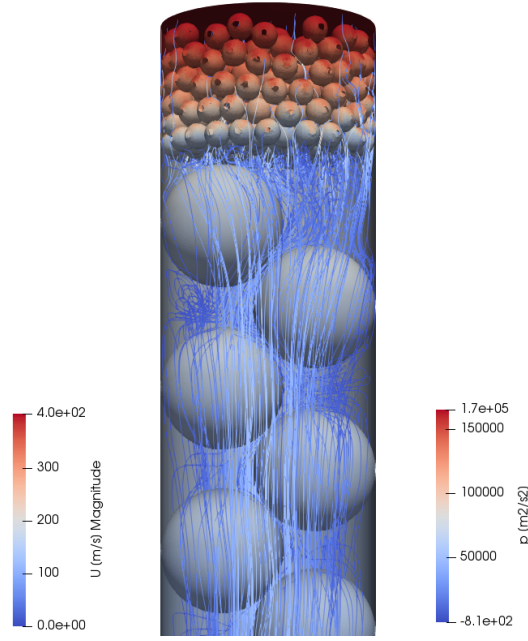


**Figure 4.2:** Front view of case D3 highlighting meandering fluid flow.

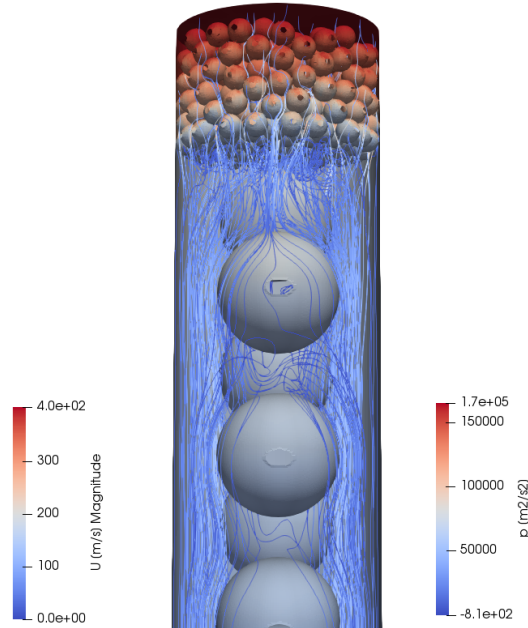


**Figure 4.3:** Side view of case D3 highlighting fluid passing the particles in a straight manner perpendicular to the plane through the pellet centres.

One notable difference between the simulative pressure drop obtained at laminar and turbulent flow would be that the simulative pressure drop approaches values closer to 0 in laminar flow as compared to larger values observed in this work (cf. Fig. 4.1c). The greater values of pressure drop associated in this work is owing to a high superficial fluid velocity flowing through the SPSR to achieve turbulent flow. Since pressure drop is directly proportional to superficial velocity (cf. Eq. 3.13), it would stand to reason that greater-than-zero values of pressure drop would be obtained even at high diameter aspect ratios from this work. It should be noted that



porosity and diameter aspect ratio are not linearly related with a porosity maximum at  $D/d = 1.67$  [52].

Lastly, Fig. 4.1d suggests an increase in pressure drop with increasing scaling factor  $s = d/d_A$ , opposite of the trend observed previously in laminar flow [17]. The Case E2 present in Fernengel et al.'s study [17] was omitted due to a high time step continuity error, which eventually causes the simulation to crash.

## 4.2 Comparison to Literature

### 4.2.1 Friction Factor

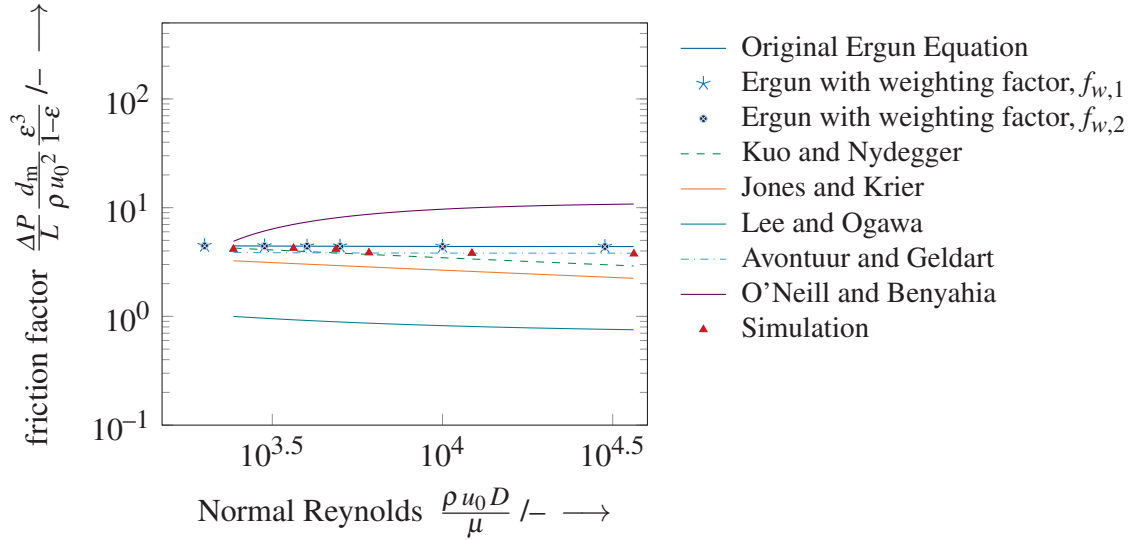


**Figure 4.4:** Simulative and Literature Friction Factor against normal Reynolds number.

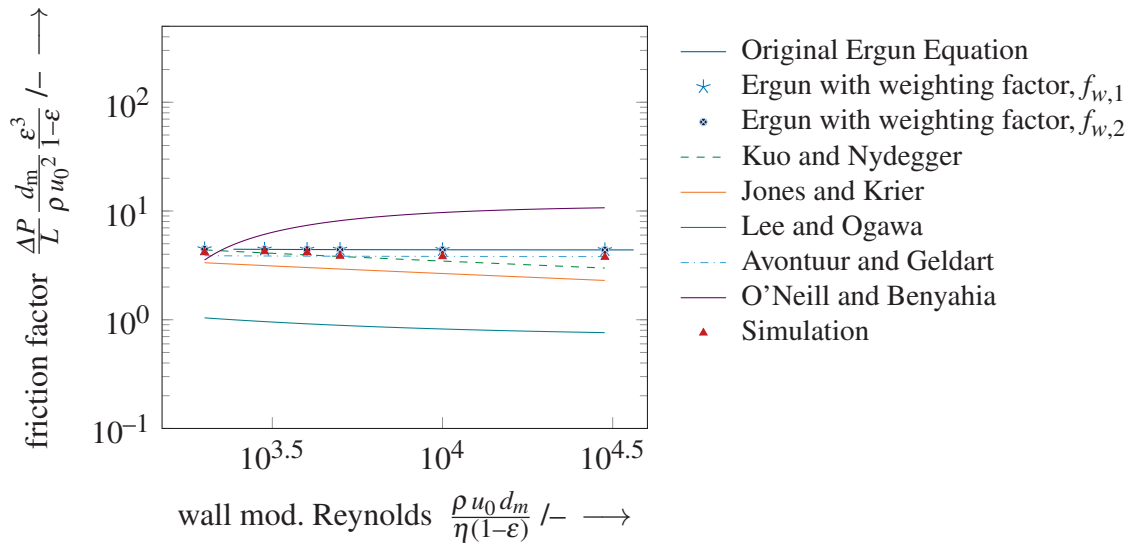


**Figure 4.5:** Simulative and Literature Friction Factor against wall modified Reynolds number.

With reference to both Figs. 4.4 and 4.5, it can be seen that the friction factor correlation as provided by Avontuur and Geldart, Kuo and Nydegger and Ergun are the most similar to the simulative friction factors obtained, with Kuo and Nydegger deviating from the simulative friction factor after a wall modified Reynolds value of  $5 \cdot 10^3$ . As mentioned by Jones and Krier, the experiments carried out by Kuo and Nydegger were performed inside a very small diameter tube having a small container diameter to bead diameter ratio ( $D/d$ ) in which frictional wall

effects are present [53]. This also meant that experiments carried out by Kuo and Nydegger were somewhat carried out in a SPSR-like environment similar to this study as the "data obtained for a test chamber diameter was too small for the bead diameter" [53]. Hence, this would attest to its similarity with the simulative friction factor.

The deviation from simulative friction factor observed beyond a wall modified Reynolds value of  $5 \cdot 10^3$  for Kuo and Nydegger would be due to the fact it is approaching (and eventually will) surpass its range of validity for friction factor ( $460 < Re < 14600$ ), hence it starts to behave abnormally as it approaches its upper friction factor limit.

Despite being outside its range of applicability, the friction factor provided by the Ergun equation (ref. Tab. 3.2, Figs. 4.4 and 4.5) lands close to the simulative friction factor obtained, with a slight over-prediction in friction factor values. A possible explanation for this would be the similarity between the friction factor equation applied in this study (cf. Eq. 3.10) and the Ergun equation. The friction factor utilised in this work, as well as those enforced by Avontuur and Geldart, Kuo and Nydegger, Jones and Krier are Ergun-based correlations. Accordingly, each of them are based off the Ergun equation with changes made mostly to the Ergun coefficients and to the related exponents. Looking at both Figs. 4.4 and 4.5, friction factors obtained from these Ergun-based correlations are the most similar to simulative results. Thus, it is plausible that the Ergun equation is largely similar to simulative friction factor values for the reason that the simulative friction factor is a Ergun-based correlation.

On the opposite end of the spectrum, a comparison with the friction factor correlation provided by Lee and Ogawa against the simulative values points to it severely under-predicting the friction factor obtained from simulations. In an attempt to create a correlation that holds true over a wide range of Reynolds number and has a simple physical meaning, Lee and Ogawa [54] proposed an all-encompassing coefficient for a packed bed to include the effects of Reynolds number and various parameters, with the assumption that flow behaviour is represented by  $Re^{-n}$ , with  $n$  being a function of voidage ( $\epsilon$ ). Though the proposed correlation was largely valid in laminar flow ( $1 < Re < 1000$ ), greater mean errors of upwards to 40% were observed in turbulent flow ( $10^3 < Re < 10^6$ ) with respect to experimental data [54]. Thus, its deviation from simulative friction factor values became apparent.

A reason for the extreme deviation from simulative friction factor observed in O'Neill and Benyahia was due to the fact that the  $D/d$  value used in the base case A was outside the valid range of  $5 < D/dp < 25$  suitable for use in O'Neill and Benyahia. This correlation was initially included for the sole purpose of demonstrating what would happen should a correlation be applied outside its range of applicability for its friction factor. However, interestingly enough, its corresponding pressure drop correlation values is the closest to parity when viewed on a parity plot in Fig. 4.7 in the next subsection.

Furthermore, it is important to note that the friction factor correlations provided by Erdim et al. [8] are mostly valid for normal Reynolds, and not wall modified Reynolds. As such, the data presented in Fig. 4.5 may not be an entirely fair comparison of between simulative and literature friction factor values. However, a plot of friction factor against normal Reynolds has also shown similar trends (Fig. 4.4), indicating that plotting the friction factor against wall modified Reynolds or normal Reynolds will not drastically affect observed trends.

Viewing both Fig. 4.5 and 4.4, it was found that the original Ergun equation and its weighting factor counterparts overestimate the friction factor relative to the simulative values obtained in turbulent flow. Also, the effects of applying a weighting factor on the Ergun equation (be it  $f_{w,1}$  or  $f_{w,2}$ ) for the calculation of friction factor appears to be minimal, yielding similar, if not equal to results obtained with the original Ergun equation. However, the consequence of applying weighting factors on the Ergun equation is much more impactful when computing for pressure drop and will be elaborated further below.

It is unfortunate however, that the article for O'Neill and Benyahia, Avontuur and Geldart, Kuo and Nydegger, Ergun could not be retrieved. As such, it is difficult to explain their deviation (or similarities) to the simulative friction factor obtained.

### 4.2.2 Parity Plots

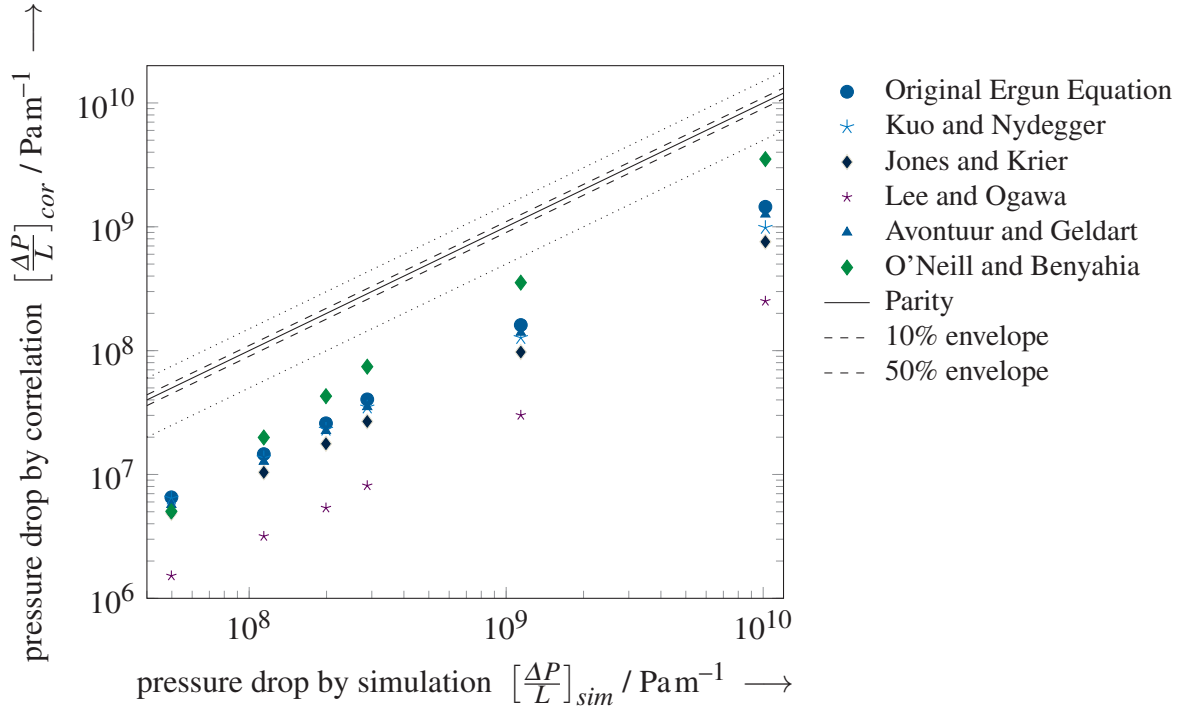


**Figure 4.6:** Parity plot for normal Reynolds in turbulent region, correlations obtained from Erdim et al. [8].

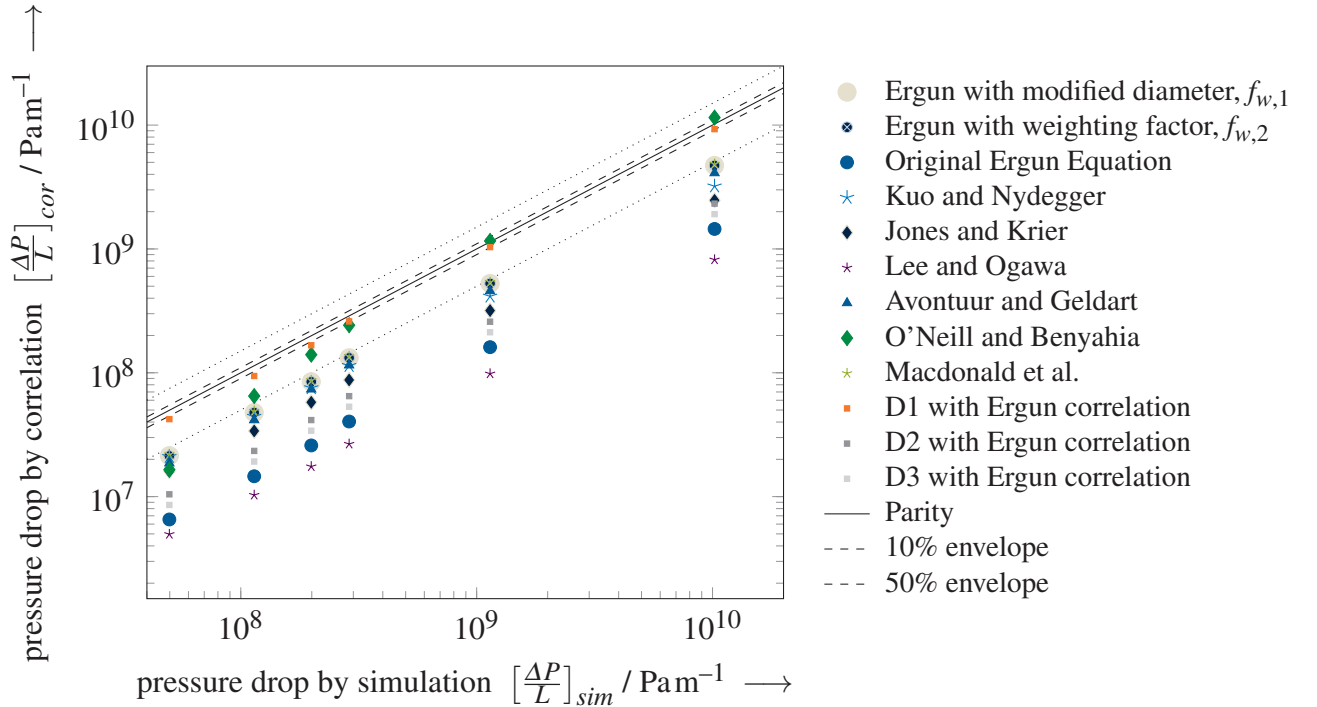


**Figure 4.7:** Parity plot for wall modified Reynolds in turbulent region, correlations obtained from Erdim et al. [8].

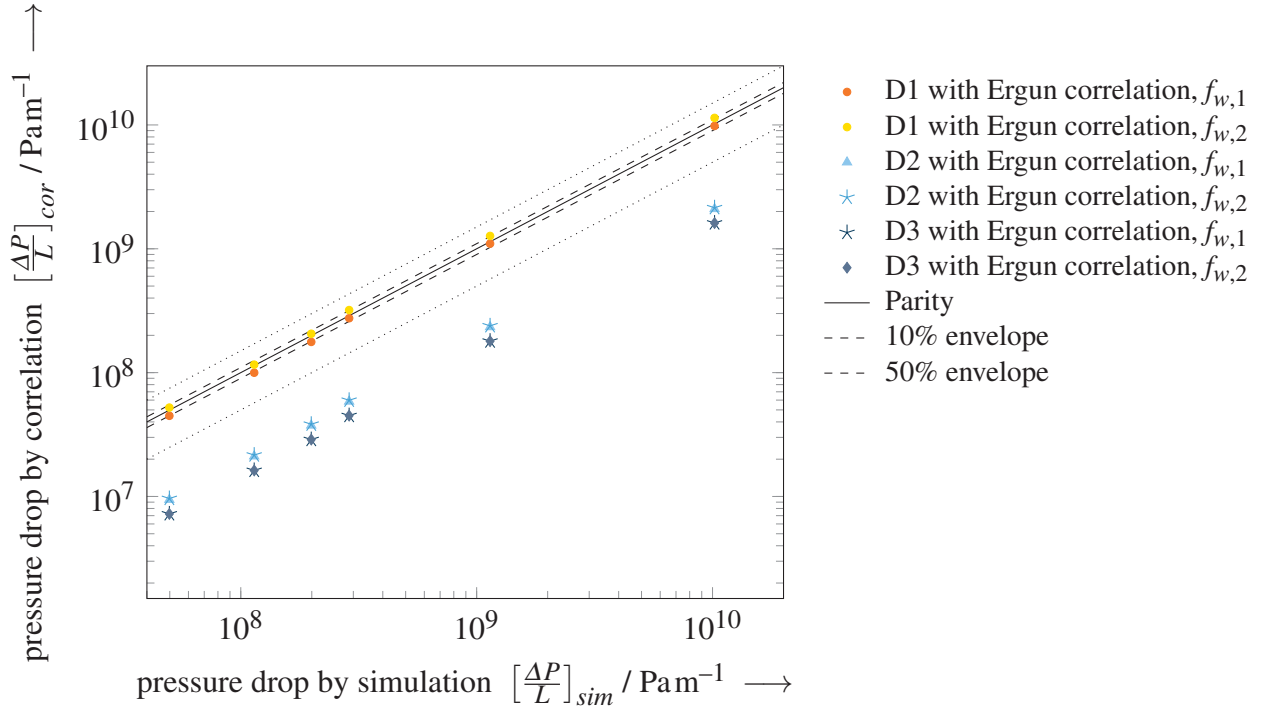


**Figure 4.8:** Parity plot showing the effects of weighting factors on cases with varying diameter aspect ratios, correlations obtained from Erdim et al. [8].

Fig. 4.7 compares pressure drop predictions by common literature correlations (cf. Erdim et al. [8]) and cases with different diameter aspect ratios using the Ergun correlation with the obtained simulation results. Interestingly enough, the pressure drop literature correlation which was closest to the simulative values was found to be O'Neill and Benyahia, having the smallest mean deviation of 23.07%. This may indicate that the inapplicability in friction factor may not necessarily be linked to an inaccurate pressure drop correlation obtained (cf. Equation 6 in Tab. 3.2).

Similar to the trends observed in Fernengel's simulations performed in laminar flow, the original Ergun equation [14] once again underestimates the pressure drop by far owing to it excluding the effects of the confining wall also in turbulent flow. Plotting a similar parity plot against normal Reynolds shifts all literature pressure drop correlation values further away from parity, with even the pressure drop correlation from O'Neill and Benyahia being shifted outside of the  $\pm 50\%$  envelope as can be seen from Fig. 4.6. It should be noted that in spite of these shifts, the general trend of which pressure drop correlation remains the closest to parity is unchanged when comparing Fig. 4.7 and 4.6.

It can be observed that most of the pressure drop correlations from literature as provided by Erdim et al. [8] provide a poor prediction for pressure drop in turbulent flow within a SPSR with outliers deviating by or greater than  $\pm 50\%$ , and greatest deviation linked to the correlation provided by Lee and Ogawa.

There are two possible reasons attributing to the deviation from simulative pressure drop values obtained with Lee and Ogawa. The first (and the most probable) reason would be due to application of the pressure drop formula (cf. Eq. 3.15, Montillet et al. ) with an already flawed friction factor values obtained earlier with reference to Fig. 4.5. Doing so may have caused errors to propagate, thereby explaining its great deviation from simulative pressure drop values. Secondly, the correlation from Lee and Ogawa was derived using an experimental model containing a packed bed with uniform spheres [54]. Although a comparison of experimental and correlation values obtained was made by Lee and Ogawa [54], the exact dimensions of the experimental packed bed in question was not provided in the work. As such, it is unclear whether its deviation from simulative pressure drop values observed in this work is owing to an inaccurate pressure drop correlation proposed, or that its deviation is a result of the difference in reactor geometries which it is conducted in.

Strikingly similar pressure drop values between Macdonald et al. [55] and the modified Ergun equation were obtained with reference to Fig. 4.7. This is expected as the friction factor correlation provided by Macdonald et al. is a modification of the Ergun equation to fit smooth and rough particles. Macdonald et al. utilised two friction factor Reynolds number correlations, the nondimensional Forchheimer equation of Ahmed and Sunada (A-S equation) and the modified Ergun equation. Both correlations were extensively tested with a large number of experimental data. Despite parameters not being well established, strong fitting of values between the A-S equation and experimental data was still observed and it was concluded that the physical model underlying the equation of A-S was more than adequate [55]. Despite successes observed with the A-S equation, the modified equation of Ergun (dubbed as the M-E Eq.) was still recommended by Erdim et al, and is applied here owing to its superiority in predicting the friction factor across a wide range of porosities ( $0.36 < \varepsilon < 0.92$ ). Furthermore, the M-E equation is adequate for a wide variety of unconsolidated porous media, which is akin to the catalytic pellets present in this simulation. The claim of a  $\pm 50\%$  deviation from experimental results when using this correlation [55] was also proved to be true as the results fell within the  $\pm 50\%$  envelope referencing Fig. 4.7.

Utilising the equivalent diameter proposed by Scott et al. [4] once again shifts the predicted values notably closer to parity, as observed in the scatter points "Ergun with modified diameter,  $f_{w,1}$ ".

However, pressure drop correlations obtained for SPSRs with diameter aspect ratios other than  $D/d = 1.25$  differ significantly, with a mean deviation from simulative pressure drop values corresponding to 12.87%, 78.30% and 82.18% (D1, D2 and D3 respectively). With reference to Fig. 4.7, and residence time being constant, the diameter aspect ratio appears to be inversely proportional to pressure drop correlation. With a decreased  $D/d$  value of 1.125 corresponding to Case D1, significant increases in pressure drop correlation values were observed, shifting

values within or close to the 10% envelope region. In comparison the largest diameter aspect ratio of  $D/d = 1.75$  corresponding to Case D3 yielded significantly reduced values of pressure drop, producing a smaller pressure drop with respect to the original Ergun equation.

A reason for this phenomenon would be the second main flow direction that passes the particles perpendicular to the plane through the pellet centres, mentioned earlier in the results section above. With increased diameter aspect ratios, more fluid is able to flow through this second flow path thus leading to higher bed porosities and hence decreased pressure drop values.

Since the data points collected are within the area of turbulent flow, the suggested correlation is centred on the Ergun equation [14]. Following the approach by Fernengel et al. [17], a weighting factor ( $f_w$ ) is introduced to the surface of the confining wall in the modified equivalent diameter expression in an attempt to shift Ergun-related correlations closer to simulative values, thereby resulting in:

$$d_m = \frac{6V_p}{S_p + f_w S_w} \quad (4.1)$$

On the first attempt, marked as 'Ergun with modified diameter,  $f_{w,1}$ ' in Fig. 4.7, the diameter aspect ratio of the SPSR is affiliated to the base case value of  $D/d = 1.25$  such that the weighting factor becomes:

$$f_{w,1} = \frac{1.25d}{D} \quad (4.2)$$

This shifts the predicted pressure drops further towards parity, with some values approaching the 50% envelope. A notable difference this time round with the application of  $f_{w,1}$  to the SPSR with the smallest considered diameter aspect ratio D1 shifts all values closer to parity within the  $\pm 10\%$  envelope, having a mean deviation of 7.60%, as opposed to steering away as with laminar flow [17]. For each considered SPSR configuration, optimal weighting factors were established independently, which were then used to match an empirical equation according to the aspect ratio of the diameter, culminating in a second weighting factor [17]:

$$f_{w,2} = 0.736 \frac{D}{d} - 14.7 \left(1 - \frac{d}{D}\right)^{3.74} + 4.8 \left(\frac{D}{d}\right)^{-17.5} \quad \text{for } 1.125 \leq \frac{D}{d} \leq 1.75 \quad (4.3)$$

The terms in the equation were selected to resemble dependency on the diameter aspect ratio and the porosity of the SPSR geometry. Fernengel et al. have seen successes in the reduction of mean deviation to simulative pressure drop upon applying  $f_{w,2}$  to the Blake-Kozeny pressure drop correlation in laminar flow [17]. The effects of the second weighting factor on the Ergun equation for turbulent flow scenarios appears to have varying successes across different reactor geometries in the reduction of mean deviation with respect to data obtained from the first weighting factor.



Referencing Fig. 4.7, it can be seen that irregardless of reactor geometries, the application of any proposed weighting factor ( $f_{w,1}$  or  $f_{w,2}$ ) to the original Ergun equation will induce a shift towards parity, identical to what was observed in laminar flow [17]. Another similar trend arises when comparing the data obtained with the Ergun correlation obtained with  $f_{w,1}$  and  $f_{w,2}$ : the shifting-towards-parity effects of  $f_{w,2}$  with the Ergun equation is more pronounced in SPSRs with lower diameter aspect ratios (D1) as compared to higher diameter aspects ratios (D2 and D3). This is substantiated with a higher difference of 3.54% obtained between  $f_{w,1}$  and  $f_{w,2}$  in Case D1, as opposed to a lower difference of  $<1\%$  in cases D2 and D3. This can be validated visually from Fig. 4.8.

The values of the optimal individual weighting factors, as well as the two proposed expressions for  $f_{w,1}$  and  $f_{w,2}$ , are presented in Fig. 4.9.

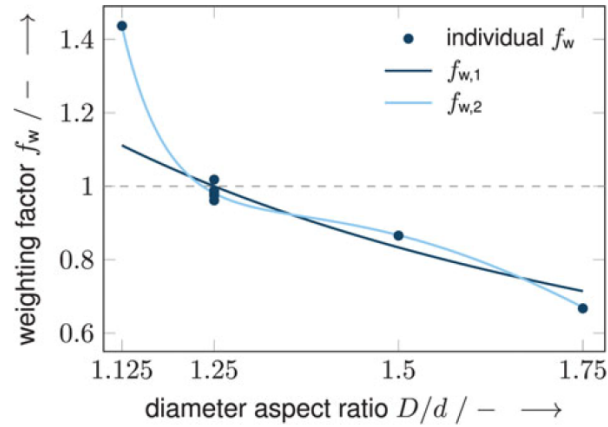


**Figure 4.9:** Wall surface weighting factor as a function of diameter aspect ratio. Taken from Fernengel et al. [17]

From a wall surface weighting factor plot shown in Fig. 4.9 (taken from Fernengel et al. [17]), the observation stated previously can be verified as it can be seen that difference between  $f_{w,2}$  and  $f_{w,1}$  is much more pronounced at lower diameter aspect ratios, and less so at increased diameter aspect ratios. This points to the confining wall effect being more prominent at small diameter aspect ratios due to a high constriction of the free cross-sectional area [17].

In such constricted areas, significant portions of the wall surface are in contact with gas traveling at its full velocity, while other areas of the pellets are situated in sluggish flow regions, i.e. near to touch points with other pellets or walls, and thus cannot produce a decrease in pressure [17]. Conversely, with increasing diameter aspect ratios, two flow channels form in the plane perpendicular to where the particles touch the wall on opposite sides leading to a reduction in flow rate through these channels hence generating reduced pressure drop [17].

Thus, these results point to a need for the inclusion of the wall surface area with a weighting factor as function of diameter aspect ratio in the Ergun equation for a more accurate prediction of pressure drop of SPSRs in turbulent flow. While a multitude of literature friction factor and pressure drop correlation exists, more specialised correlations (preferably considering wall effects) formulated from experiments or simulations conducted in SPSRs will have to be made before an accurate prediction of pressure drop in SPSRs can be done.

## 5 Conclusion

The simulated pressure drop across SPSRs mostly follows the expected trends previously established by Fernengel et al. in laminar flow [17] upon varying fluid viscosity, flow velocity, diameter aspect ratio and reactor scale. Exceptions to the expected trends occurred with the variation of superficial velocity and scaling factor, in which the expected behaviour of pressure drop obtained with an increase in scaling factor was completely opposite to what was previously obtained in laminar flow [17].

Although the graph obtained with superficial velocity in this work projects an exponential curve with increasing pressure drop as opposed to an expected linear trend as previously observed in laminar flow [17], its behaviour is still substantiated with findings presented by Müller et al. [51], who had also obtained similar results with a SPSR in turbulent flow within a simulative environment.

When considering the effects of the confining wall in turbulent flow, Ergun-based correlations provides a means to predict pressure drop behaviour.

The choice of base case geometry this time however, does not correspond to an agreement of most literature pressure drop correlations, with many of them underpredicting the pressure drop by 50% or greater. Scott et al.'s [4] method and addition of a weighting factor to the surface of the confining wall in the equivalent diameter formulation was followed, shifting results that are closer to parity in conjunction with the Ergun equation.

Adopting a straightforward factor ( $f_{w,1}$ ) based solely on the diameter aspect ratio on the base case, and cases with different diameter aspect ratio resulted in a substantial improvement in accuracy. Using a more detailed mathematical formulation for the weighting factor as a function of the diameter aspect ratio comprising of five designed parameters ( $f_{w,2}$ ) across cases with varying diameter aspect ratios yielded results with differing successes in the prediction of pressure drop in SPSRs. However, it was still concluded nonetheless in the limiting case of SPSRs with differing diameter aspect ratios that the use of either suggested weighting factors will inadvertently push pressure drop correlation values to simulation values.

Overall, this work has mostly achieved its goal in obtaining simulative pressure drop in turbulent flow of the previously investigated SPSRs variations proposed by Fernengel et al. [17]. Further fine-tuning of the *fvSolution* code 3.2 used is necessary to handle more turbulent flows (corresponding to increased wall modified Reynolds value) as well as cases with a larger reactor scale. The obtained results were compared and contrasted against a deluge of pressure drop correlations from literature, most of which underpredicting the simulative pressure drop values. Thus, there is a need for more specialised pressure drop correlations to be developed (ideally through experiments in an SPSR) should a more accurate prediction of pressure drop in SPSRs be sought after.

Having more in-depth knowledge about crucial plant design parameters such as pressure drop behaviour will lead to better physical models of SPSRs following plug-flow behaviour to be developed. This may in turn lead to SPSRs to be adopted in the industries as a safer, cheaper and less labour intensive alternative to conventional packed bed reactors for the performance testing of catalysts.

# A Bibliography

- [1] R. Warnecke, *Biomass and bioenergy* **2000**, 18, 489–497.
- [2] F. Menter, T. Esch in 16th Brazilian Congress of Mechanical Engineering (COBEM), Vol. 109, **2001**, p. 650.
- [3] F. R. Menter, M. Kuntz, R. Langtry, *Turbulence heat and mass transfer* **2003**, 4, 625–632.
- [4] D. Scott, W. Lee, J. Papa, *Chemical Engineering Science* **1974**, 29, 2155–2167.
- [5] A. Klyushina, K. Pacultová, L. Obalová, *Reaction Kinetics Mechanisms and Catalysis* **2015**, 115, 651–662.
- [6] R. Moonen, J. Alles, E.-j. Ras, C. Harvey, J. A. Moulijn, *Chemical Engineering & Technology* **2017**, 40, 2025–2034.
- [7] A. Müller, J. Kanz, S. Haase, K. Becker, H.-M. Vorbrodt, *Chemical Engineering and Processing: Process Intensification* **2017**, 113, 2–13.
- [8] E. Erdim, Ö. Akgiray, İ. Demir, *Powder Technology* **2015**, 283, 488–504.
- [9] J. Fernengel, L. Bolton, O. Hinrichsen, *Chemical Engineering Journal* **2019**, 373, 1397–1408.
- [10] M. H. Al-Dahhan, M. P. Dudukovic, *Chemical Engineering Science* **1994**, 49, 5681–5698.
- [11] M. H. Al-Dahhan, Effects of high pressure and fines on the hydrodynamics of trickle-bed reactors. **1995**.
- [12] W. Wammes, S. Mechielsen, K. Westerterp, *Chemical engineering science* **1991**, 46, 409–417.
- [13] R. A. Holub, Hydrodynamics of trickle bed reactors. **1992**.
- [14] S. Ergun, *Chemical Engineering Progress* **1952**, 48, 89–94.
- [15] F. Blake, *Transactions of the American Institute of Chemical Engineers* **1922**, 14, 3.
- [16] J. Kozeny, *Akademie Wissenschaften Wien* **1927**, 136, 271.
- [17] J. Fernengel, L. Bolton, O. Hinrichsen, *Chemical Engineering & Technology* **2020**, 43, 172–178.

- 
- [18] D. Mehta, M. Hawley, *Industrial & Engineering Chemistry Process Design and Development* **1969**, 8, 280–282.
- [19] W. Reichelt, *Chemie Ingenieur Technik* **1972**, 44, 1068–1071.
- [20] B. Eissfeld, K. Schnitzlein, *Chemical Engineering Science* **2001**, 56, 4321–4329.
- [21] R. M. Fand, M. Sundaram, M. Varahasamy, Incompressible fluid flow through pipes packed with spheres at low dimension ratios, **1993**.
- [22] Z. Guo, Z. Sun, N. Zhang, M. Ding, J. Wen, *Chemical Engineering Science* **2017**, 173, 578–587.
- [23] H. Heinemann, *Catalysis Today* **1994**, 22, 281–293.
- [24] S. Sie, *AIChE Journal* **1996**, 42, 3498–3507.
- [25] H. A. San, *Water Research* **1989**, 23, 647–654.
- [26] H. Gierman, *Applied Catalysis* **1988**, 43, 277–286.
- [27] B. Blocken, *Catholic University of Leuven (Belgium)* **2004**.
- [28] G. Chen, Q. Xiong, P. J. Morris, E. G. Paterson, A. Sergeev, Y. Wang, *Notices of the AMS* **2014**, 61, 354–363.
- [29] G. Alfonsi, *Applied Mechanics Reviews* **2009**, 62.
- [30] M. Pisarenco, B. van der Linden, A. Tijsseling, E. Ory, J. Dam, *Journal of Offshore Mechanics and Arctic Engineering* **2011**, 133.
- [31] H. Tennekes, J. L. Lumley, J. L. Lumley, et al., *A first course in turbulence*, MIT press, **1972**.
- [32] J. Hinze, *Turbulence*. McGraw-Hill Publishing Co, **1975**.
- [33] D. Wilcox, *Turbulence modelling for CFD*. Tech. rep., ISBN 0-9636051-0-0, DCW Industries Inc., La Canada, California, **1993**.
- [34] F. Menter in 23rd Fluid Dynamics, Plasmadynamics, and Lasers Conference, **1993**, p. 2906.
- [35] F. R. Menter, *AIAA Journal* **1994**, 32, 1598–1605.
- [36] W. Rodi in 29th Aerospace sciences meeting, **1991**, p. 216.
- [37] C. Chen, S. Jaw, *Washington DC* **1998**.
- [38] H. Schlichting, *Boundary layer theory*, Vol. 960, Springer, **1960**.
- [39] F. M. White, I. Corfield, *Viscous fluid flow*, Vol. 3, McGraw-Hill New York, **2006**.
- [40] B. Blocken, T. Stathopoulos, J. Carmeliet, *Atmospheric Environment* **2007**, 41, 238–252.
- [41] I. Nezu, A. Tominaga, *Asakura Shoten* **2000**, 130–133.
- [42] S. M. Salim, S. Cheah in Proceedings of the international multiconference of engineers and computer scientists, Vol. 2, Hong Kong, **2009**, pp. 2165–2170.

- [43] F. Liu, *Proceedings of CFD with OpenSource Software* **2016**, 1–33.
- [44] H. Tabor, H. Jasak, C. Fureby, *Computational Physics* **1998**, 6.
- [45] Blender Foundation, Blender 2.76b, software package (2015).
- [46] E. Coumans, URL: <http://www.cs.uu.nl/docs/vakken/mgp/assignment/Bullet> **2012**.
- [47] OpenFOAM: User Guide v1912: k-omega Shear Stress Transport (SST), **2016-2017**.
- [48] J. Kozeny, *Royal Academy of Science Vienna Proc. Class I* **1927**, 136, 271–306.
- [49] M.-D. Lee, S.-H. Shen, T.-K. Chung, C.-K. Kuei, *AIChE Journal* **1984**, 30, 639–641.
- [50] A. Montillet, E. Akkari, J. Comiti, *Chemical Engineering and Processing: Process Intensification* **2007**, 46, 329–333.
- [51] A. Müller, J. Petschick, R. Lange, *Procedia Engineering* **2012**, 42, 1189–1201.
- [52] V. M. Govindarao, K. V. Ramrao, A. V. Rao, *Chemical Engineering Science* **1992**, 47, 2105–2109.
- [53] D. P. Jones, H. Krier, Gas flow resistance measurements through packed beds at high Reynolds numbers, **1983**.
- [54] J. S. Lee, K. Ogawa, *Journal of Chemical Engineering of Japan* **1994**, 27, 691–693.
- [55] I. Macdonald, M. El-Sayed, K. Mow, F. Dullien, *Industrial & Engineering Chemistry Fundamentals* **1979**, 18, 199–208.

# Declaration

The submitted thesis was supervised by Prof. Dr.-Ing. Kai-Olaf Hinrichsen.

## **Affirmation**

Hereby, I affirm that I am the sole author of this thesis. To the best of my knowledge, I affirm that this thesis does not infringe upon anyone's copyright nor violate any proprietary rights. I affirm that any ideas, techniques, quotations, or any other material, are in accordance with standard referencing practices.

Moreover, I affirm that, so far, the thesis has not been forwarded to a third party nor is it published. I obeyed all study regulations of the Technische Universität München.

## **Remarks about the internet**

Throughout the work, the internet was used for research and verification. Many of the keywords provided herein, references and other information can be verified on the internet. However, no sources are given, because all statements made in this work are fully covered by the cited literature sources.

Garching, March 16, 2020

---

Yong Sook Prasit Attavit